



**AFRL-RB-WP-TR-2012-0112**

# **PHYSICS-BASED DESIGN OF MICRO AIR VEHICLES**

**Richard D. Snyder, Philip Beran, and Raymond Kolonay**

**Design and Analysis Methods Branch  
Structures Division**

**APRIL 2012  
Interim Report**

**Approved for public release; distribution unlimited.**

*See additional restrictions described on inside pages*

**STINFO COPY**

**AIR FORCE RESEARCH LABORATORY  
AIR VEHICLES DIRECTORATE  
WRIGHT-PATTERSON AIR FORCE BASE, OH 45433-7542  
AIR FORCE MATERIEL COMMAND  
UNITED STATES AIR FORCE**

## NOTICE AND SIGNATURE PAGE

Using Government drawings, specifications, or other data included in this document for any purpose other than Government procurement does not in any way obligate the U.S. Government. The fact that the Government formulated or supplied the drawings, specifications, or other data does not license the holder or any other person or corporation; or convey any rights or permission to manufacture, use, or sell any patented invention that may relate to them.

This report was cleared for public release by the USAF 88<sup>th</sup> Air Base Wing (88 ABW) Public Affairs Office (PAO) and is available to the general public, including foreign nationals. Copies may be obtained from the Defense Technical Information Center (DTIC) (<http://www.dtic.mil>).

AFRL-RB-WP-TR-2012-0112 HAS BEEN REVIEWED AND IS APPROVED FOR PUBLICATION IN ACCORDANCE WITH THE ASSIGNED DISTRIBUTION STATEMENT.

\*//Signature//

---

RICHARD D. SNYDER  
Research Aerospace Engineer  
Design and Analysis Methods Branch  
Structures Division

//Signature//

---

DENIS P. MROZINSKI  
Chief  
Design and Analysis Methods Branch  
Structures Division

//Signature//

---

JAMES A. KOCHER  
Chief  
Structures Division  
Air Vehicles Directorate

This report is published in the interest of scientific and technical information exchange, and its publication does not constitute the Government's approval or disapproval of its ideas or findings.

\*Disseminated copies will show “//Signature//” stamped or typed above the signature blocks.

REPORT DOCUMENTATION PAGE				Form Approved OMB No. 0704-0188	
<p>The public reporting burden for this collection of information is estimated to average 1 hour per response, including the time for reviewing instructions, searching existing data sources, gathering and maintaining the data needed, and completing and reviewing the collection of information. Send comments regarding this burden estimate or any other aspect of this collection of information, including suggestions for reducing this burden, to Department of Defense, Washington Headquarters Services, Directorate for Information Operations and Reports (0704-0188), 1215 Jefferson Davis Highway, Suite 1204, Arlington, VA 22202-4302. Respondents should be aware that notwithstanding any other provision of law, no person shall be subject to any penalty for failing to comply with a collection of information if it does not display a currently valid OMB control number. <b>PLEASE DO NOT RETURN YOUR FORM TO THE ABOVE ADDRESS.</b></p>					
1. REPORT DATE (DD-MM-YY) April 2012		2. REPORT TYPE Interim		3. DATES COVERED (From - To) 01 October 2008 – 30 September 2011	
4. TITLE AND SUBTITLE PHYSICS-BASED DESIGN OF MICRO AIR VEHICLES				5a. CONTRACT NUMBER In-house	
				5b. GRANT NUMBER	
				5c. PROGRAM ELEMENT NUMBER 61102F	
6. AUTHOR(S) Richard D. Snyder, Philip Beran, and Raymond Kolonay				5d. PROJECT NUMBER 2307	
				5e. TASK NUMBER	
				5f. WORK UNIT NUMBER A0F00B	
7. PERFORMING ORGANIZATION NAME(S) AND ADDRESS(ES) Design and Analysis Methods Branch (AFRL/RBSD) Structures Division Air Force Research Laboratory, Air Vehicles Directorate Wright-Patterson Air Force Base, OH 45433-7542 Air Force Materiel Command, United States Air Force				8. PERFORMING ORGANIZATION REPORT NUMBER AFRL-RB-WP-TR-2012-0112	
9. SPONSORING/MONITORING AGENCY NAME(S) AND ADDRESS(ES) Air Force Research Laboratory Air Vehicles Directorate Wright-Patterson Air Force Base, OH 45433-7542 Air Force Materiel Command United States Air Force				10. SPONSORING/MONITORING AGENCY ACRONYM(S)  AFRL/RBSD	
				11. SPONSORING/MONITORING AGENCY REPORT NUMBER(S) AFRL-RB-WP-TR-2012-0112	
12. DISTRIBUTION/AVAILABILITY STATEMENT Approved for public release; distribution unlimited.					
13. SUPPLEMENTARY NOTES PAO Case Number: 88ABW-2011-5838; Clearance Date: 03 Nov 2011. Report contains color.					
14. ABSTRACT Micro air vehicles, especially those that use flapping wings for propulsion and control, are characterized by complex, time-dependent, nonlinear interactions amongst a variety of physical disciplines. These interactions must be carefully controlled to attain desired levels of performance, but the number and range of parameters that describe possible micro aircraft is extremely large, poorly explored, and inadequately understood. Aerodynamic, structural, kinematic, and mechanical parameters are relevant and may be strongly coupled with each other. In this report, we describe a multidisciplinary optimization methodology that can be used to isolate combinations of parameters that elicit beneficial aeroelastic interactions from flapping wings. This methodology relies on disciplinary models that are tailored to the physics of each problem considered and on highly efficient solution strategies suitable for design optimization. We then report on results from the application of this methodology to three problems involving flapping wings in either hover or steady forward flight. In each case, we identify physical mechanisms that can be used to achieve significant gains in relevant performance metrics such as force production and power consumption.					
15. SUBJECT TERMS micro air vehicles, flapping, hover, aeroelasticity, optimization					
16. SECURITY CLASSIFICATION OF:			17. LIMITATION OF ABSTRACT: SAR	18. NUMBER OF PAGES 56	19a. NAME OF RESPONSIBLE PERSON (Monitor) Richard D. Snyder 19b. TELEPHONE NUMBER (Include Area Code) N/A
a. REPORT Unclassified	b. ABSTRACT Unclassified	c. THIS PAGE Unclassified			

## ABSTRACT

Micro air vehicles, especially those that use flapping wings for propulsion and control, are characterized by complex, time-dependent, nonlinear interactions amongst a variety of physical disciplines. These interactions must be carefully controlled to attain desired levels of performance, but the number and range of parameters that describe possible micro aircraft is extremely large, poorly explored, and inadequately understood. Aerodynamic, structural, kinematic, and mechanical parameters are relevant and may be strongly coupled with each other. In this report, we describe a multidisciplinary optimization methodology that can be used to isolate combinations of parameters that elicit beneficial aeroelastic interactions from flapping wings. This methodology relies on disciplinary models that are tailored to the physics of each problem considered and on highly efficient solution strategies suitable for design optimization. We then report on results from the application of this methodology to three problems involving flapping wings in either hover or steady forward flight. In each case, we identify physical mechanisms that can be used to achieve significant gains in relevant performance metrics such as force production and power consumption.



## TABLE OF CONTENTS

Abstract .....	ii
List of Figures .....	iv
List of Tables.....	vi
Introduction .....	1
Methodology .....	3
A. Aerodynamics Methods.....	3
1. Quasi-Steady Blade Element Aerodynamics .....	3
2. UVLM Aerodynamics.....	4
3. Navier-Stokes Aerodynamics.....	5
B. Nonlinear Structural Mechanics .....	7
C. Kinematics .....	9
1. Berman and Wang Kinematics.....	9
2. Spline-Based Kinematics .....	10
D. Optimization .....	11
1. Gradient-Based Method .....	11
2. Genetic Algorithm.....	11
Applications .....	13
A. Aeroelastic Shape, Structure, and Kinematics Design and Parameter Exploration .....	13
B. Conceptual Design of Compliant Mechanisms for Flapping Wings.....	19
1. Optimizing for Thrust Alone.....	20
2. Optimizing for Thrust and Rolling Moment .....	25
C. Influence of Wing Stiffener Arrangements on Flapping Wing Performance.....	29
Conclusions .....	39
Acknowledgments.....	40
References .....	41

## LIST OF FIGURES

Figure 1. Quasi-steady blade element model verification: force generation of a rigid flapping wing.....	4
Figure 2. Slit camera view comparison of UVLM results with water tunnel experimental data for a pure plunging motion. ....	5
Figure 3. Navier-Stokes test case configuration composed of a rigid airfoil and a flexible plate. .	6
Figure 4. Variations in predicted pitch and phase angles for changes in Strouhal number for the Navier-Stokes test case. ....	7
Figure 5. Comparison of an insect wing and a manufactured wing for a flapping MAV.....	8
Figure 6. Structural beam model validation of a clamped elbow beam subjected to an impulse load at its corner. ....	9
Figure 7. Structural shell model validation of a clamped plate subjected to flapping motion.....	9
Figure 8. Berman and Wang flapping wing kinematics and coordinate systems. ....	10
Figure 9. Finite element discretization of a nonlinear beam, with variable chord length and thickness for each element. ....	14
Figure 10. Optimal chord and thickness distributions for a flapping wing in hover.....	17
Figure 11. Optimal kinematic flapping motions for a flapping wing in hover. ....	17
Figure 12. Time-periodic power history for baseline and optimal designs of a flapping wing in hover.....	18
Figure 13. Contributions to the power for optimal case C.....	18
Figure 14. Rigid and flexible motion of the wingtip for case C.....	19
Figure 15. Schematic of an actuated flapping wing in forward flight.....	20
Figure 16. Optimal topologies for a flapping-wing compliant actuation mechanism. Hatched areas are clamped. Cases 1-3 have fixed supports; cases 4 and 5 have variable supports. ....	23
Figure 17. Variation in flapping performance due to changes in compliant actuator input force ( $\omega = 100$ rad/sec).....	25
Figure 18. Variation in flapping performance due to changes in compliant actuator input frequency ( $f = 15$ N).....	25
Figure 19. Two scenarios for symmetric and unsymmetric actuation of left and right wings using a compliant mechanism.....	26
Figure 20. Optimal compliant actuation mechanisms designed for maximum rolling moment and a trimming cycle-averaged thrust coefficient.....	28
Figure 21. Phase diagrams of flapping rotation due to input actuation (positive angles correspond to wing tips up). ....	28

## LIST OF FIGURES, cont'd

Figure 22. First four iterations of an example cellular division process. ....	30
Figure 23. Sample wing finite element model for studying the effect of stiffener arrangements on aeroelastic performance. Membrane elements are outlined with thin black lines and beam elements are shown as thick blue and red lines. ....	31
Figure 24. Single-objective optimal designs for a flexible wing skeleton. ....	33
Figure 25. Single-objective optimal designs for a stiff wing skeleton. ....	34
Figure 26. Thrust-power Pareto front for the flexible case. ....	34
Figure 27. Thrust-power Pareto front for the stiff case. ....	35
Figure 28. Thrust-power-lift Pareto front for the stiff configuration. ....	35
Figure 29. Out-of-plane wing deformation throughout the flapping cycle of the thrust-optimal stiff topology design. ....	36
Figure 30. Out-of-plane wing deformation throughout the flapping cycle of the power-optimal stiff topology design. ....	37
Figure 31. Out-of-plane deformation throughout the flapping cycle of the lift-optimal stiff topology design. ....	38

## LIST OF TABLES

Table 1. Baseline values and side constraints for the shape, structure, and kinematics design variables. ....	15
Table 2. Parameters for the shape, structure, and kinematics optimization of a flapping wing in hover.....	16
Table 3. Cases for the shape, structure, and kinematics optimization of a flapping wing in hover. ....	16
Table 4. Structural parameters for the compliant actuation mechanism design.....	22
Table 5. Aerodynamic parameters for the compliant actuation mechanism design.....	22
Table 6. Summary of performance metrics for optimal topologies for a flapping-wing compliant actuation mechanism.....	23
Table 7. Summary of optimal compliant actuation mechanisms designed for maximum rolling moment and a trimming cycle-averaged thrust coefficient.....	28
Table 8. Material and geometric properties of the membrane wing and stiffeners.....	33

## INTRODUCTION

Micro air vehicles (MAVs) are small autonomous, semi-autonomous, or remotely piloted aircraft. Given their particularly small size and their ability to operate in close spaces, they are envisioned to perform a variety of missions that are unavailable or inaccessible to conventionally sized aircraft. Intelligence, surveillance, and reconnaissance missions are of particular interest. MAVs are also contemplated as micro munitions, capable of delivering low-collateral weapons into restricted spaces. Many other missions are possible, as MAVs have the potential to match the variety of performance characteristics exhibited in the natural world by flying insects, birds, and mammals. However, an inadequate understanding of the complex, nonlinear, and multidisciplinary physics that underlie flight at these scales complicates realization of such capabilities.

Engineers from many organizations around the globe have already successfully constructed and flown a wide variety of small-scale robotic aircraft. These vehicles range in size from small birds upwards, use fixed-wing, rotary, or flapping-wing layouts, and exhibit varying levels of endurance, controllability, and agility. AeroVironment, Inc. and the Defense Advanced Research Projects Agency (DARPA), for example, have recently demonstrated a remotely piloted two-wing flapping MAV weighing 19 g with a wingspan of 16 cm<sup>1</sup>. Called the "Nano Hummingbird," the concept demonstrator is capable of controlled flight and hover and has a sufficient level of maneuverability to establish a desired orientation within a horizontal plane, to transition between hover and forward flight, and to fly through a normal-sized doorway. The designers, like others before them, met their flight test milestones primarily through extensive experimental testing and iterative improvement of flight test hardware. While this approach was used successfully in the DARPA program, it is limited by the degree of physical insight that the designers can bring to the workbench. Given the multidisciplinary and nonlinear character of the physics, such an approach is expected to be quite limited. We believe that a thorough understanding of aeroelastic behavior at small scales and an associated physics-based design process are needed to realize effective MAV designs.

Engineers engaged with a MAV design will be driven to choose a structural layout and propulsive mechanism by the particulars of the mission requirements. A fixed wing design will be best for some missions, a rotary wing design for other missions, and a flapping-wing design for still others. Quantitative assessment of the relative strengths of each configuration type is needed to help guide future designs. However, we have, for the purposes of this study, chosen to focus on flapping-wing designs. The physics of flapping flight are arguably least well understood, and flapping wings offer significant potential for agility.

The physics of flapping-wing MAVs is challenging due to the nonlinear and multidisciplinary character of the system. As is well known, small changes in a system parameter can sometimes produce large changes in the system response of a nonlinear system. Also, couplings between two or more physical disciplines can give rise to energy transfers that significantly influence system outputs. These effects are often deleterious to performance objectives, but can occasionally be beneficial. The challenge is to identify those parameters that have the greatest impact on the system performance, exploit beneficial nonlinearities and

multidisciplinary interactions, and avoid substantial detrimental effects. Multidisciplinary optimization techniques provide a systematic approach for exploring the parameter space in systems where sufficiently accurate numerical models are available to represent system behavior. For MAVs, this requires an aeroelastic modeling capability informed by both theory and experiment that can capture key physical couplings between the unsteady aerodynamics, structural mechanics, kinematics, and actuation mechanics.

There are many challenges associated with modeling flow fields around small, agile aircraft. The flow physics are highly nonlinear and inherently dynamic. In fact, MAVs depend upon unsteady flow mechanisms to generate forces sufficient for flight. Operating at low Reynolds numbers of  $10^5$  or less, viscosity and turbulence can be important factors, and vortical flow features are dominant. Wing interactions with the fuselage or other wings can be strong due to the vehicle geometry and the flapping kinematics. Aeroelastic behavior can only be properly characterized when the aerodynamics are modeled accurately. On the other hand, the strength of aeroelastic interactions depends upon a large number of system configuration parameters defining geometry, structure, kinematics, controls, and other characteristics. Exploring this large parameter space is costly and requires fast simulations. This gives rise to a situation in which different levels of aerodynamic modeling fidelity are appropriate. Low and medium fidelities are needed to explore the parameter space and identify regions of interesting physics. High-fidelity methods are needed to fully characterize the aerodynamics associated with beneficial physical interactions.

Small-scale aircraft, particularly flapping-wing MAVs, generally use very thin wings. These might be constructed of plies of composite material or of an even thinner flexible membrane material. Beams or battens are often incorporated into the wings to provide additional stiffness. Structural deformations in such wings can be large, especially for flapping, and must be considered to be nonlinear. In some cases, the true structure can be reduced to a set of equivalent nonlinear beams. In general, however, MAV wings should be treated as nonlinear plates or membranes, possibly combined with nonlinear beam elements for stiffening.

## METHODOLOGY

We use multidisciplinary optimization to explore flapping-wing MAV physics, with an eye towards leveraging beneficial interactions that may exist between elements of the flapping system. In particular, we have been concerned with multidisciplinary couplings between the unsteady aerodynamics, nonlinear structure, flapping-wing kinematics, and flapping actuation mechanism. Computational optimization requires both accurate and timely models for each of these physical disciplines. Key physical interactions and the sensitivity of those interactions to variations in select system parameters must be captured adequately so that the optimization process can reveal useful parameter combinations. This drives the researcher towards high-fidelity models. On the other hand, when considering many system parameters, the optimization process requires a large number of potentially costly analyses and exploration of the parameter space can become intractable. The multidisciplinary optimization approach, therefore, requires that the physical models be carefully chosen so as to capture the necessary physical features while minimizing computational cost. These decisions are problem dependent, so it is useful to have, for each discipline, a collection of models of varying fidelity to draw upon. This allows the investigative method to be tailored to the particular problem under consideration.

This section will describe the major physical models and numerical methods that have been developed and/or used in our research. The following section will show applications of these various methods to problems relevant to flapping-wing MAVs.

### A. Aerodynamics Methods

The unsteady and nonlinear aerodynamics of flapping wings represent perhaps the most challenging aspect of aeroelastic modeling for multidisciplinary optimization. Complicated flow features are usually present and, in many cases, improving performance depends on wisely controlling these features. This suggests that high-fidelity models such as the Reynolds-averaged Navier-Stokes (RANS) and large eddy simulation Navier-Stokes (LES) methods are best suited to MAV applications. However, it has been shown through comparisons with experiments that, for certain problems, lower-fidelity aerodynamics methods are able to capture the major vortical flow features associated with flapping while requiring significantly reduced computational resources. These lower-order methods, therefore, have been used extensively in multidisciplinary studies of flapping physics.

#### *1. Quasi-Steady Blade Element Aerodynamics*

We use an internally developed implementation of the aerodynamic model discussed by Berman and Wang<sup>2-4</sup>. Following the blade element assumption, 3D lifting surfaces are divided along the span into a number of chordwise segments. The total force is obtained by summing the forces calculated on each segment. The force acting on an individual element is found by a model formulated to study free-falling plates and is equal to the sum of four components<sup>5,6</sup>.

$$F = F_{\text{circulation}} + F_{\text{added mass}} + F_{\text{viscous dissipation}} + F_{\text{rotating frame}} \quad (1)$$

The expression for the circulation and viscous terms involve translational and rotational force coefficients and a drag coefficient that are typically taken from experimental measurements of wind tunnel models, birds, or insects.

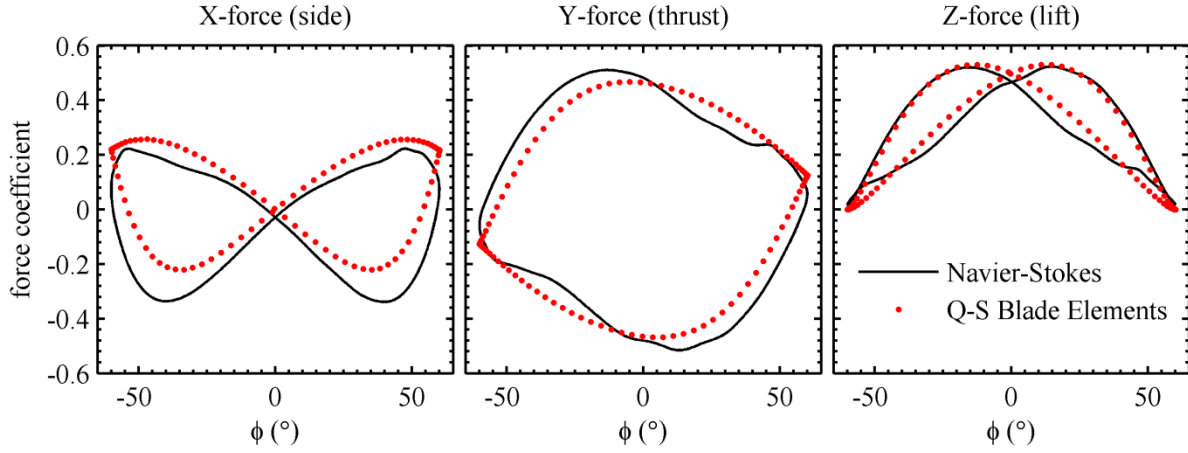


**Figure 1. Quasi-steady blade element model verification: force generation of a rigid flapping wing.**

It only takes seconds to execute a quasi-steady blade element simulation, yet results can be quite accurate for many problems. For example, Figure 1 shows a good agreement between force generation curves obtained by the blade element and Navier-Stokes methods for a flapping half-ellipse planform. The wing, with a 50 mm span and an 18.2 mm mean chord, was flapped at a frequency of 26 Hz with the following prescribed kinematics:

$$\begin{aligned}\phi &= \frac{\pi}{3} \cos(2\pi ft) \\ \theta &= 0 \\ \eta &= -\frac{\pi}{4} \sin(2\pi ft) + \frac{\pi}{2}\end{aligned}\tag{2}$$

## 2. UVLM Aerodynamics

The unsteady vortex lattice method (UVLM) offers a balance between the computational efficiency of a quasi-steady blade element method and the physical accuracy of a Navier-Stokes method. The equations are simpler and faster to solve than the Navier-Stokes equations. While viscosity is ignored and flow separation must be modeled, UVLM is able to capture the major vortical flow features associated with dynamic MAV flows. We have created both 2D and 3D UVLM solvers<sup>7,8</sup>. The UVLM is well suited to incorporating models for turbulence, and we have completed this integration in 2D<sup>9</sup>.

Karamcheti and Katz and Plotkin described the basics of this method<sup>10,11</sup>. It is developed using Kelvin's circulation theorem, which states that the circulation around a closed curve moving with a fluid remains constant with time for an inviscid barotropic flow with conservative



body forces. Lifting bodies are represented as a discrete collection of bound vortices and an equivalent number of control points. At each moment in time, circulation strengths of the bound vortices are determined by enforcing flow tangency at the control points. For a given vortex filament, the induced velocity  $\mathbf{v}$  is given by the Biot-Savart law as:

$$\mathbf{v} = \frac{1}{4\pi} \int \frac{\Gamma d\mathbf{s} \times \mathbf{r}}{|\mathbf{r}|^3} \quad (3)$$

where  $\Gamma$  is the circulation strength of the filament,  $\mathbf{r}$  is the displacement vector from the filament to the point of interest, and  $d\mathbf{s}$  is a differential element of the filament. At each iteration in time, vortices are shed from the lifting surface and convected into a wake so as to preserve a net circulation strength of zero for the complete system.

We have shown that the UVLM gives good agreement with data collected from pitching and plunging airfoils in a water tunnel<sup>12</sup>. For example, Figure 2 shows a comparison of a plunging SD7003 airfoil. In this case, the pure plunging occurs at a reduced frequency of  $k = 3.93$  with an amplitude of 9.2% of the airfoil chord length. In this view, the vertical axis shows the solution at a fixed location one chord length behind the trailing edge and the horizontal axis represents time, increasing to the right. Flow in the tunnel is recorded using injected blue dye and the computational vortices are traced using colored dots. Similar qualitative comparisons were found for other airfoil motions and reduced frequencies.

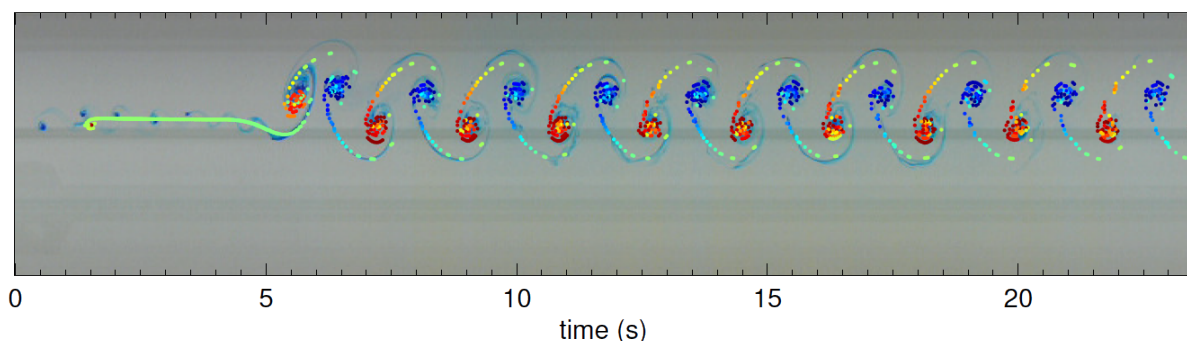


**Figure 2. Slit camera view comparison of UVLM results with water tunnel experimental data for a pure plunging motion.**

### 3. Navier-Stokes Aerodynamics

Low-order aerodynamics models such as the blade element and UVLM methods described above make simplifying assumptions that might cause numerical predictions to miss important physical behavior. Higher-order methods such as the Reynolds-averaged Navier-Stokes (RANS) and large eddy simulation (LES) are appropriate for such situations. Even where lower-order methods can suitably capture the relevant physics, Navier-Stokes methods can be useful for conducting detailed inspections of the aerodynamic behavior in narrow regions of interest in the parameter space.

We have developed a coupled, aeroelastic solver based on the OVERFLOW Navier-Stokes flow solver and a custom mode-based structural solver<sup>13</sup>. The solver uses an explicit coupling between the flow solver and structural model. OVERFLOW is a compressible Navier-Stokes flow solver for structured overset solution domains. It is based on a finite difference formulation and is capable of fifth-order spatial accuracy using the Weighted Essentially Non-Oscillatory (WENO) scheme and second-order temporal accuracy using dual time stepping<sup>14,15</sup>. For low Mach number solutions or solutions encompassing mixed Mach number flows, the code incorporates low Mach number preconditioning<sup>16</sup>. The implemented preconditioning is time-accurate when used with a dual time stepping solution. Multibody and moving body solution capabilities are accommodated using a chimera, or overset, solution approach<sup>17</sup>. Arbitrary rigid-body motion may be prescribed and a 6DOF model is available for computing rigid-body motion due to aerodynamic forces. The OVERFLOW family of solvers has some build-in capability to model flexible bodies and we extended the program for application to MAVs with flexible beam-like wings.

The OVERFLOW-based aeroelastic solver has been tested against a two-dimensional case based on the work of Heathcote and Gursul, who examined the influence of structural flexibility on thrust coefficient and propulsive efficiencies for a heaving airfoil in water, across a range of Strouhal and Reynolds numbers. The experimental setup utilized an airfoil with an aluminum teardrop stiffener along the first third of the chord and a flexible steel plate for the last two-thirds of the airfoil, as shown in Figure 3 together with a view of near-body mesh as the body deforms.

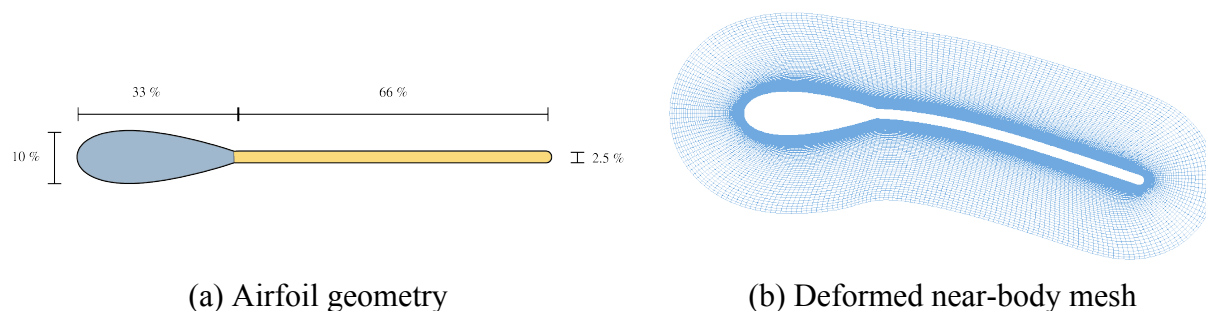


**Figure 3. Navier-Stokes test case configuration composed of a rigid airfoil and a flexible plate.**

Figure 4 compares numerical and experimental results for the following conditions: Reynolds number  $Re = 9000$ , Mach number  $M_\infty = 0.05$ , plate thickness  $b/c = 0.0056$ , and a forced plunging of the rigid teardrop according to  $h(t) = 0.05c(1 - e^{-t/\tau}) \cos(\omega t)$ . Force histories provide good agreement with experiment. However, the explicit modal solutions overpredict the tip deflection, as represented by the pitching angle, defined as the angle between the freestream and a line connecting the leading and trailing edges of the foil. This variation in pitching angle is accompanied by an associated shift in phase angle between the leading and trailing edge motion. The linear mode-based structural solver is expected to overpredict the true nonlinear response, so using a better, more accurate structural solver would likely eliminate some of the disagreement with experimental data.

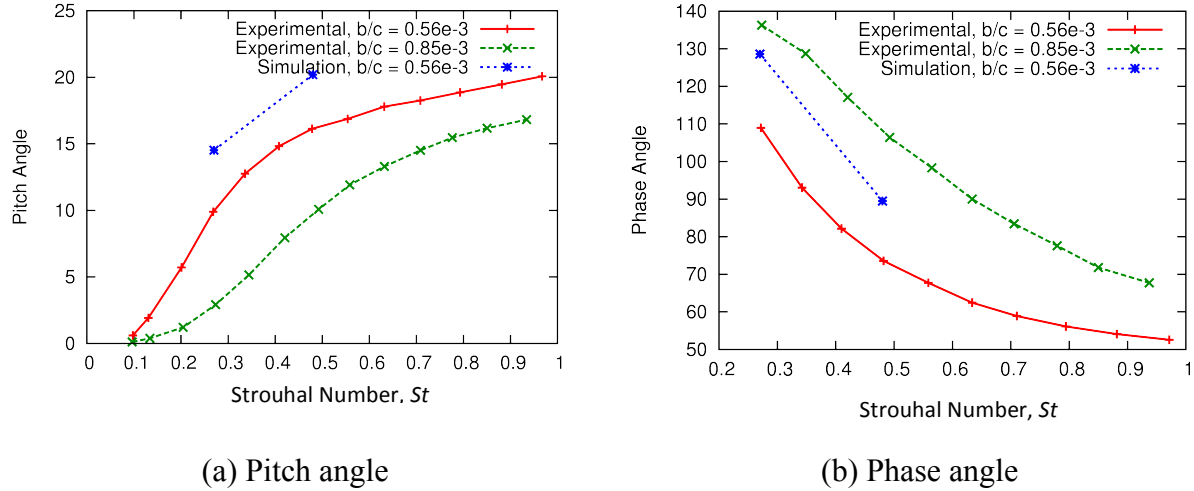


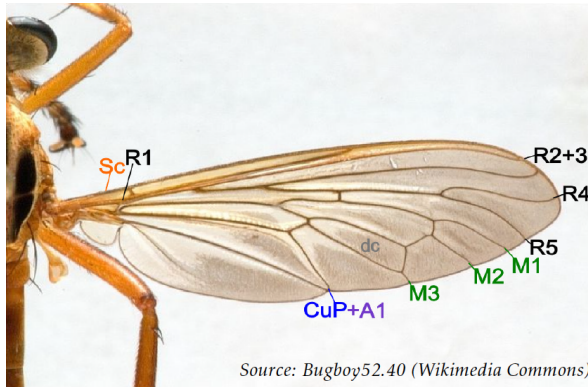
**Figure 4. Variations in predicted pitch and phase angles for changes in Strouhal number for the Navier-Stokes test case.**

Immersed boundary methods have also been used to study problems that involve flapping<sup>19-21</sup>. The method is well-suited to such flows because the body does not need to conform to the fluid mesh, thereby eliminating the need for the remeshing process associated with unstructured solvers or the dynamic hole cutting associated with overset solvers. In exchange for a simplified handling of the computational mesh, special boundary conditions must be used to incorporate the body into the flow solution. We have worked with Balaras and Dong to incorporate immersed boundary codes into our high-order aerodynamics tool suite.

## B. Nonlinear Structural Mechanics

Small-scale aircraft, particularly flapping-wing MAVs, generally use very thin wings. These might be constructed of plies of composite material or of an even thinner flexible membrane material. Beams or battens are often incorporated into the wings to provide additional stiffness. As shown in Figure 5, insect wings, with their vein and cell structure, often inspire manufactured wing designs. Structural deformations in such wings can be large, especially for flapping, and must be considered to be nonlinear. In some cases, the true structure can be reduced to a set of equivalent nonlinear beams. Here, variational asymptotic beam sectional analysis can be used to facilitate construction of an equivalent nonlinear beam<sup>22,23</sup>. In general, however, MAV wings should be treated as nonlinear plates or membranes, possibly combined with nonlinear beam elements for stiffening. We have developed nonlinear finite element solvers that are based on a corotational approximation of the updated Lagrangian procedure<sup>24-26</sup>. Both two-dimensional (2D) beam and three-dimensional (3D) shell finite element formulations are available. In the corotational approach, the total displacement of an element is divided into a component due to rigid-body motion and a component due to pure displacement<sup>27</sup>. The contribution of the rigid motion is removed from the element computations, leaving only the elastic deformation. This makes it possible to consider problems with large rotations but small strains. In three dimensions, a three-node triangular shell element is used that combines an optimal membrane element (OPT)

and a discrete Kirchhoff theory (DKT) plate bending element<sup>28</sup>. The effect of nonlinear stress stiffening is added to the co-rotational formulation by including a geometric stiffness matrix. Limited verification and validation of these solvers has been completed and have shown good agreement with theory.



(a) Fly wing



(b) Manufactured wing

**Figure 5. Comparison of an insect wing and a manufactured wing for a flapping MAV.**

In Figure 6, the 3D nonlinear beam model is compared with results from the commercial finite element solver ABAQUS. A beam with a 90° elbow and a solid circular cross-section is clamped at one end and subjected to an impulse point load at its corner. Inertial and aerodynamic forces are zero, structural damping is zero, and the force impulse lasts for the duration of the simulation. The time history of the displacement at the free end of the elbow compares well with the commercial code and demonstrates the ability of the solver to accurately capture large 3D bending and twisting dynamics<sup>29</sup>.

The 3D nonlinear shell model is compared with ABAQUS in Figure 7. For this study, the feathering axis runs through the mid-chord of the wing and the entire root is clamped, as indicated on the diagram within the figure<sup>24</sup>. Kinematic motions for this problem are given by the expressions

$$\begin{aligned}\theta &= (1 - e^{-2000t^2}) \cdot (-\pi/4) \sin(\omega t) \\ \psi &= (1 - e^{-2000t^2}) \cdot (\pi/4) \sin(\omega t - \pi/2)\end{aligned}\tag{4}$$

with a flapping frequency of  $\omega = 100$  rad/sec and no viscous damping. Results are given in terms of the normalized transverse and spanwise displacement at point A, located at the leading-edge tip of the wing. Displacements are measured with respect to the body-attached coordinate system and, therefore, reflect structural deformations, but not the prescribed rigid body motions due to flapping. The match between the shell model and ABAQUS is very good. The strongly nonlinear transverse deformations are of the same magnitude as the wing length, resulting in a significant foreshortening effect that is accurately captured by the shell model.

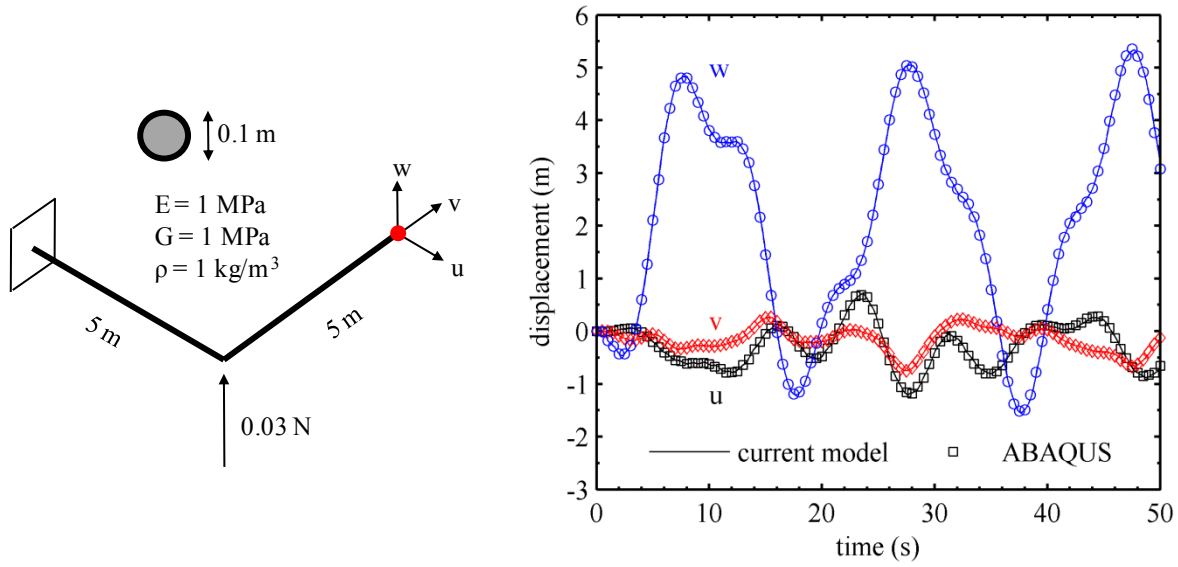


**Figure 6. Structural beam model validation of a clamped elbow beam subjected to an impulse load at its corner.**

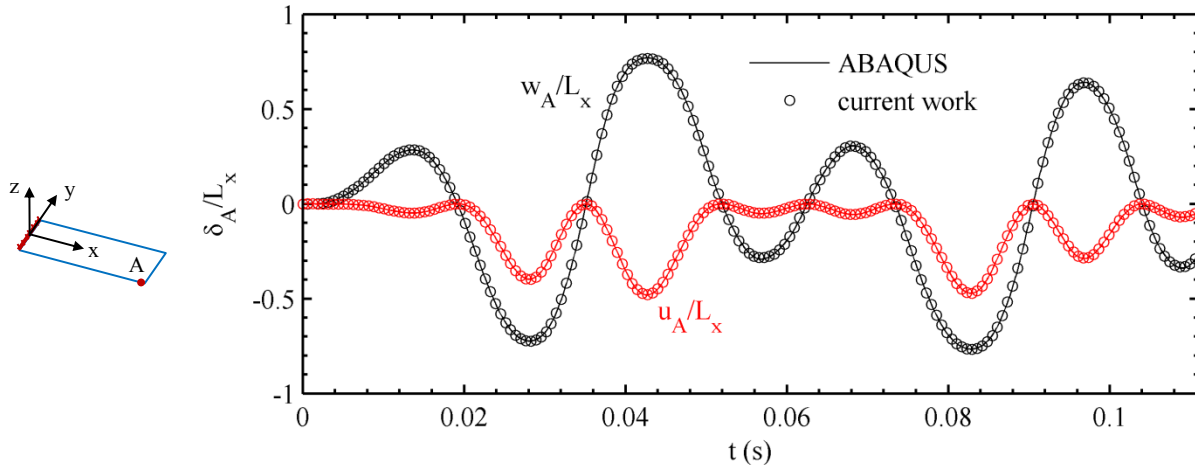


**Figure 7. Structural shell model validation of a clamped plate subjected to flapping motion.**

### C. Kinematics

Rigid motion in a flapping-wing vehicle can be described in several ways. We have relied on a couple of descriptions.

#### 1. Berman and Wang Kinematics

Following Berman and Wang<sup>30</sup>, we consider a flapping wing that is able to rotate in three degrees of freedom about a hinge at the root of the wing. The degrees of freedom are the azimuth

angle  $\phi$ , elevation angle  $\theta$ , and pitch angle  $\eta$ , as shown in Figure 8. The equations for these angles are taken to be:

$$\begin{aligned}\phi &= \phi_m \frac{\sin^{-1}(K_\phi \sin(2\pi ft))}{\sin^{-1}(K_\phi)} \\ \theta &= \theta_m \cos(2\pi ft + \theta_s) + \theta_0 \\ \eta &= \eta_m \frac{\tanh(C_\eta \sin(2\pi ft + \eta_s))}{\tanh(C_\eta)} + \eta_0\end{aligned}\tag{5}$$

These equations contain a total of ten parameters. The parameter  $K_\phi$  may vary between 0 for a sinusoidal waveform and 1 for a triangular waveform. The parameter  $C_\eta$  varies between 0 for a sinusoidal waveform and infinity for a step function.

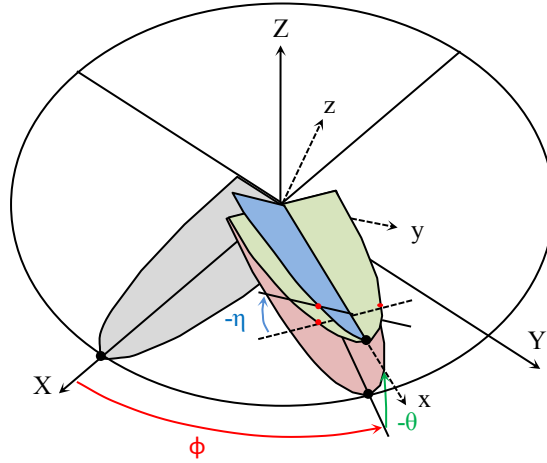


**Figure 8. Berman and Wang flapping wing kinematics and coordinate systems.**

## 2. Spline-Based Kinematics

Basis splines (B-splines) can be used to represent kinematic degrees of freedom in a very general way. B-splines offer localized control of the path and the number of possible defining parameters is essentially unbounded<sup>31</sup>. Introduce a knot vector  $\mathbf{T}$  with  $m$  non-decreasing real elements. Each kinematic degree of freedom  $S(t)$  can be expressed as a linear combination of basis functions:

$$S(t) = \sum_{i=0}^{m-p-2} P_i N_{i,p}(t), \quad t \in [t_p, t_{m-p-1}]\tag{6}$$

Here,  $p$  is the order of the spline. The  $P_i$  are called the control points, and there are  $m - p - 1$  such points. Their positions become the parameters that describe the kinematic formulation. The B-spline basis functions can be defined using the Cox-de Boor recursion formula:

$$\begin{aligned}
N_{i,0}(t) &= \begin{cases} 0, & t_i \leq t < t_{i+1} \\ 1, & \text{otherwise} \end{cases} \\
N_{i,p}(t) &= \frac{t - t_i}{t_{i+p} - t_i} N_{i,p-1}(t) + \frac{t_{i+p+1} - t}{t_{i+p+1} - t_{i+1}} N_{i+1,p-1}(t)
\end{aligned} \tag{7}$$

## D. Optimization

Two types of optimization algorithm are used in this effort: single-objective optimization via a gradient-based method and multi-objective optimization via a genetic algorithm. Non-gradient methods require more objective and constraint function evaluations than gradient-based methods. Gradient-based methods also have good convergence properties within the radius of convergence around an optimal point. Consequently, gradient-based methods are typically favored for problems in which the derivatives of the objective and constraints are known analytically or can be computed quickly and accurately by finite difference. Non-gradient-based methods can be preferred for problems where derivatives are unavailable or difficult to compute and for problems in which the presence of local minima confound a gradient-based search for a global optimum.

### 1. Gradient-Based Method

The optimization problem can be stated formally as

$$\begin{aligned}
&\min_x \mu(x) \\
&\text{s.t.} \\
&g(x) \leq 0 \\
&h(x) = 0 \\
&x_\ell \leq x \leq x_u
\end{aligned} \tag{8}$$

where  $\mu(x)$  is the objective function,  $g(x)$  are the inequality constraints,  $h(x)$  are the equality constraints, and  $x$  is the vector of decision variables.

The gradient-based modified method of feasible directions is used for constrained optimization problems, as implemented in the CONMIN and DOT optimization programs<sup>32,33</sup>. These programs can also use sequential linear programming and sequential quadratic programming methods for constrained optimization and Broydon-Fletcher-Goldfarb-Shanno variable metric and Fletcher-Reeves conjugate gradient methods for unconstrained optimization. These methods are iterative and require evaluation of the chosen objective function and any active constraints at each point in the optimization search. Typically, about a dozen iterations are needed to converge to an optimum solution.

### 2. Genetic Algorithm

The problem statement for a multi-objective optimization is the same as that given in (8), except that the objective function  $\mu(x)$  becomes an  $n$ -dimensional vector of functions. Instead of a unique solution, the multi-objective problem possesses a possibly infinite set of points that

together define the solution. These are called the Pareto points, and are identified as points in the objective space  $\mu^*$  for which there does not exist another feasible design objective vector  $\mu$  such that  $\mu_i \leq \mu_i^*$  for all  $i \in \{1, 2, \dots, n\}$ , and  $\mu_j < \mu_j^*$  for at least one index  $j \in \{1, 2, \dots, n\}$ .

The Non-dominated Sorting Genetic Algorithm-II (NSGA-II) is used here to solve multi-objective optimization problems via a non-gradient-based evolutionary algorithm. The method uses a fast non-dominated sorting approach to search for the Pareto front<sup>34</sup>. Elitism in the selection process speeds the solution process and also helps to prevent the loss of good solutions. As with many evolutionary algorithms, the algorithm identifies a large number of alternative solutions lying on or near the Pareto-optimal front in a single run.



## APPLICATIONS

In this section, we summarize a few applications of our multidisciplinary optimization methodology to the study of significant problems associated with flapping-wing MAVs. The reader is referred to the references given in Appendix A for other applications conducted under the auspices of this laboratory task.

### A. Aeroelastic Shape, Structure, and Kinematics Design and Parameter Exploration

The wings of animals that fly are often flexible. As with conventional aircraft, rigid wings are simply too heavy for flight, and a variety of numerical and experimental research has indicated the benevolent effects of wing flexibility for both energy and lift considerations, outside of the obvious weight savings. Insects have no muscles embedded in their wings, and so flexibility plays a passive role: adaptive feathering, cambering, and chordwise bending, and various coupling mechanisms have been found for many species<sup>35</sup>. Birds and bats are capable of active morphing, but these creatures also use passive mechanisms. Although the role of flexibility in flying animals is not fully understood, it almost certainly contributes to the extreme agility, maneuverability, and stability of biological flyers. Successful exploitation of such passive flexibility mechanisms in a mechanical flapper requires an ability to simultaneously consider changes in aerodynamic shape, flapping kinematics, and structural layout. Considering the structure alone is insufficient due to strong nonlinear couplings with fluid flow.

When designing a flapping aircraft capable of sustained stationary hovering, three objectives must be met. First, the wings must generate enough aerodynamic lift to balance the weight of the vehicle. Second, the mechanical stresses that develop within the wing structure must not lead to mechanical failure. Third, the input power to the system must be minimized. This last point is particularly important because the energy budgets onboard a MAV are expected to be extremely limited. The interaction of these objectives can be examined numerically by forming an inexpensive aeroelastic optimization capability for power minimization under trim and failure constraints<sup>29,36</sup>. The aeroelastic optimization used for this effort combines Berman and Wang aerodynamics and Berman and Wang kinematics with a nonlinear beam model based on a co-rotational approximation of the updated Lagrangian procedure. These numerical models are described in earlier sections.

The elastic wing is divided along the span into a number of beam elements with rectangular cross sections, as shown in Figure 9. The structural beam and the aerodynamic surface are considered here to be a unified object. In other words, at a given span station, the beam width and aerodynamic chord length are identical. The chord length  $c_i$  and thickness  $h_i$  of each element is allowed to change independently. The thickness of each element has a strong effect on the structural and mass properties of the wing, but will only slightly alter the aerodynamic forces through added mass terms in the Berman and Wang aerodynamics model. Conversely, the chord length of each element will have a strong effect on the aerodynamic forces, but only have a moderate impact on the structure. These dependencies are explicit; the coupled nature of the aeroelastic solver ensures that both chord and thickness distributions effect the aeroelastic equations of motion in an implicit manner. A direct method is used to evaluate the sensitivities of

the objective and constraint equations to changes in the design variables, and gradient-based optimization is used to guide the optimization process.

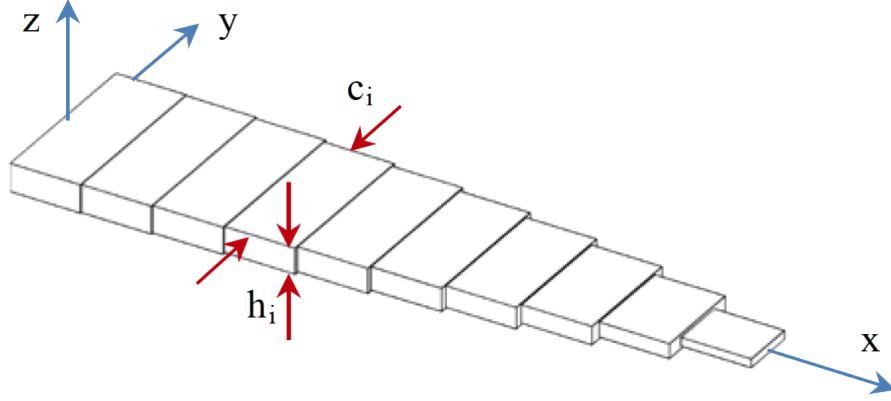


**Figure 9. Finite element discretization of a nonlinear beam, with variable chord length and thickness for each element.**

For a beam with  $N$  finite elements, there are  $2N$  design variables describing the shape and structure. There are an additional nine parameters describing the Berman and Wang kinematics, so the optimization problem has a total of  $2N + 9$  design variables:

$$\mathbf{x} = \{c_1 \quad \cdots \quad c_N \quad h_1 \quad \cdots \quad h_N \quad \phi_m \quad K_\phi \quad \theta_m \quad \theta_s \quad \theta_0 \quad \eta_m \quad \eta_s \quad \eta_0 \quad C_\eta\}. \quad (9)$$

Baseline, lower, and upper bounds for these variables is given in Table 1.

The optimization problem can be formally stated as:

$$\begin{aligned} & \min_{\mathbf{x}} p(t_{cr,1}) \\ & \text{s.t.} \\ & L_{ave} \geq L^* \\ & KS(t_{cr,2}) \leq 0 \\ & R_n = 0 \quad n = 1, \dots, N_{steps} \\ & x_{min} \leq x_e \leq x_{max} \quad e = 1, \dots, N_{DV} \end{aligned} \quad (10)$$

where  $p$  is the power required to actuate a single wing, given by the following equation:

$$p = \frac{dK_E}{dt} + \frac{dS_E}{dt} + p_{aero} \quad (11)$$

Here,  $K_E$  is the kinetic energy of the wing due to both rigid body and deformational motions,  $S_E$  is the strain energy of the beam due only to deformational motions, and  $p_{aero}$  is the aerodynamic power. It is desired to minimize the peak power draw of the system, which occurs at a time  $t_{cr,1}$ , once the motion has become periodic. It is further desired to keep the elastic stresses that develop throughout the beam below some critical failure stress. Including a stress constraint for each beam element is not desirable. However, a Kreisselmeier-Steinhauser function can be computed over the wing and a constraint applied to that value.

$$KS = \frac{1}{\kappa} \cdot \ln \left[ \sum_{n=1}^N e^{\kappa \left( \frac{\sigma_{VM}}{\sigma^*} - 1 \right)} \right] \quad (12)$$

Where  $\sigma_{VM}$  is the maximum Von Mises stress within the beam element,  $\sigma^*$  is the maximum allowable stress, and  $\kappa = 20$ . The composite  $KS$  function peaks at the critical time  $t_{cr,2}$ , at which time the function must be negative. Unlike the power objective, though,  $t_{cr,2}$  can occur at any time during the simulation, not just during the periodic flapping motion. The cycle-averaged lift force  $L$  generated by one wing must be greater than some specified value  $L^*$ . Also, all design variables must lie between side constraints, as given in Table 1. Finally, the equations of motion must be satisfied at each time step or, in other words,  $R_n = 0$  for each time step  $n$ .

**Table 1. Baseline values and side constraints for the shape, structure, and kinematics design variables.**

	$c_i$ (mm)	$h_i$ (mm)	$\phi_m$ (rad)	$K_\phi$ (-)	$\theta_m$ (rad)	$\theta_s$ (rad)
minimum	10	0.2	$-\pi/2$	0.01	$-\pi/4$	$-\pi/4$
baseline	25	0.6	$\pi/3$	0.01	0	0
maximum	60	2.5	$\pi/2$	0.50	$\pi/4$	$\pi/4$
	$\theta_0$ (rad)	$\eta_m$ (rad)	$\eta_s$ (rad)	$\eta_0$ (rad)	$C_\eta$ (-)	
minimum	$-\pi/2$	$-\pi/2$	$-\pi/2$	$-\pi/2$	0.01	
baseline	0	$\pi/4$	$\pi/2$	$-\pi/2$	0.10	
maximum	$\pi/2$	$\pi/2$	$\pi/2$	$\pi/2$	1.00	

The number of beam elements is taken to be  $N = 10$ , which gives a total of 29 possible design variables. Each flapping cycle is broken into 100 time steps, and 8 flapping cycles were found to be sufficient to develop a time-periodic aeroelastic response. The remaining system parameters are given in Table 2.

**Table 2. Parameters for the shape, structure, and kinematics optimization of a flapping wing in hover.**

Parameter	Value	Parameter	Value
$N$	10	$\rho_f$	1.225 kg/m <sup>3</sup>
Wing length	10 cm	$C_T$	1.83
Elastic modulus	70 GPa	$C_D(0)$	0.21
Shear modulus	26.9 GPa	$C_D(\pi/2)$	3.35
Wing density	2800 kg/m <sup>3</sup>	$C_R$	$\pi$
$\mathbf{C}$	$20\mathbf{M}$	$\mu_1$	0.2
$\sigma^*$	350 MPa	$\mu_2$	0
$L^*$	0.15 N	$f$	19.9 Hz

Three optimization studies are considered and are summarized in Table 3. Case A considers only the kinematic design variables and fixes the chord lengths and thicknesses of the beam elements to a baseline design, leaving 9 active design variables. Case B considers only the chord lengths and thicknesses that describe the aerodynamic and structural properties of the wing while holding the kinematics to a baseline design. This gives 20 active design variables. Finally, for case C, all variables are active.

**Table 3. Cases for the shape, structure, and kinematics optimization of a flapping wing in hover.**

Case	$N_{DV}$	Description
A	9	Optimize kinematics, fix aerodynamic and structural geometry
B	20	Optimize aerodynamic and structural geometry, fix kinematics
C	29	Optimize kinematics as well as aerodynamic and structural geometry

The optimal designs are given in Figure 10 and Figure 11. The former gives the chord length and thickness distribution along the beam for cases B and C. The shape for case A is that of the baseline. The latter figure gives the kinematic flapping motions for cases A and C. The kinematics for case B is that of the baseline. Focusing on the shape and structure, both optimal designs drop the thickness below the baseline value. The wing tip thickness for both designs is that of the lower bound on thickness, presumably to decrease the wing moment of inertia and thus the inertial power. Both designs keep the chord length of the first few beam elements near the root close to the baseline value. Larger chord lengths are used outboard for lift generation, where the translational motion is larger. Significant differences are seen between cases B and C at the wing tip, where the former pushes the length to the lower bound on chord, while the latter keeps the length at a moderate value.

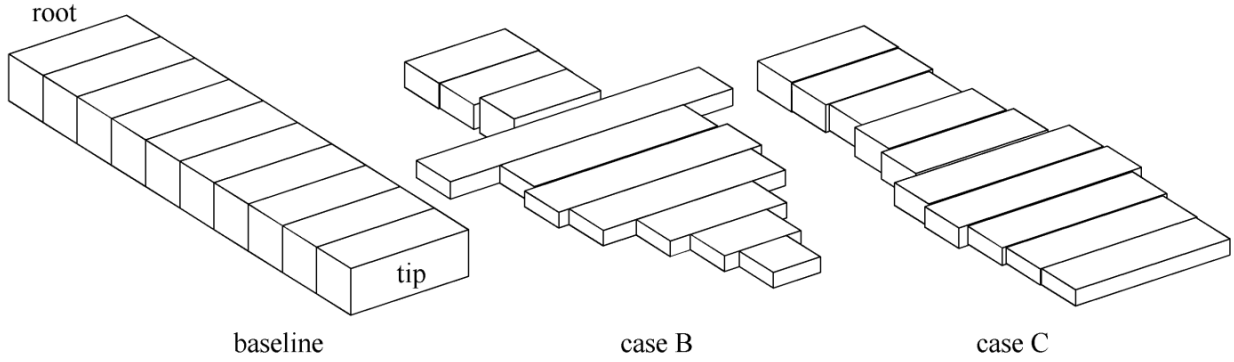


**Figure 10. Optimal chord and thickness distributions for a flapping wing in hover.**

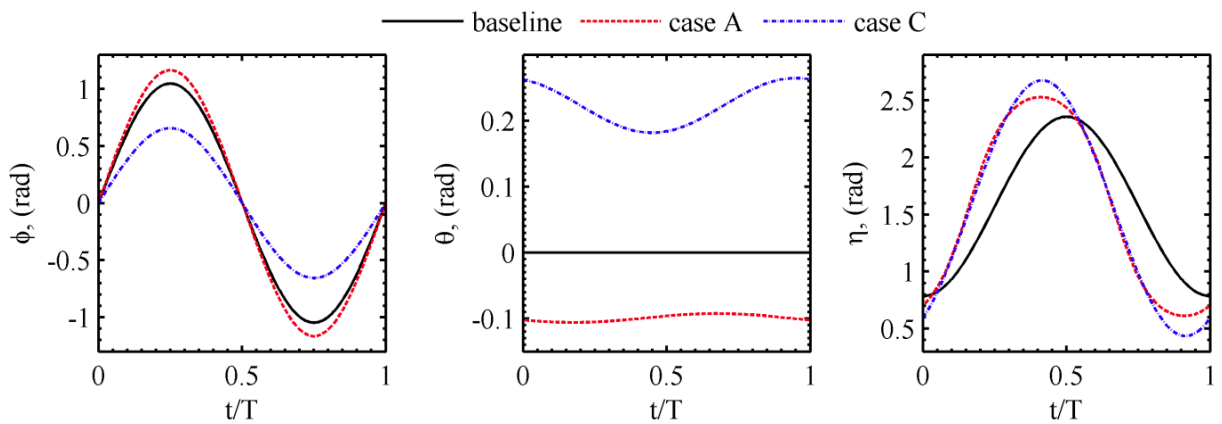


**Figure 11. Optimal kinematic flapping motions for a flapping wing in hover.**

As opposed to the shape and structural design variables, the optimizer does not significantly alter the flapping motions for power reduction. The overall out-of-phase relationship between the stroke motion  $\phi$  and the wing feathering  $\eta$  is preserved, presumably for lift generation requirements. The optimal designs use the stroke plane deviation angle  $\theta$  to push the rigid flapping motion slightly above or below the mean plane, and passive aeroelastic deformation provides further deviation. Case C is able to drop the amplitude of stroke motion significantly below the baseline value.

The time-periodic power history that results from the optimal designs is shown in Figure 12, together with that for the baseline design. Case A is unable to decrease the peak power from the baseline value in a feasible manner, as the lift constraint must be met. The kinematic motions alone were not able to provide efficient solutions. For case B, fixing the kinematic motions and permitting changes to the shape and structure provides a significant drop in peak power. For case C, also including the kinematic variables provides a still greater reduction in peak power. A plot of the terms that make up the total power for case C is instructive. In Figure 13, no single term dominates, indicating that aerodynamic and inertial forces are of similar magnitude. Drops in the kinetic energy rate, as the wing generates lift through the mid-stroke, offset peaks in the

aerodynamic power, as energy is continuously stored and released throughout the vibrating beam, attenuating the total peak value.

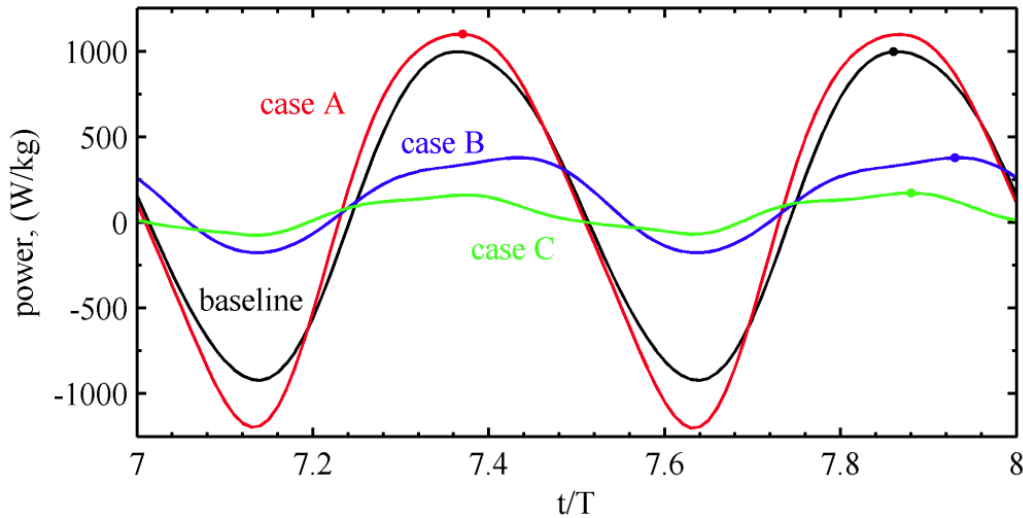


**Figure 12. Time-periodic power history for baseline and optimal designs of a flapping wing in hover.**

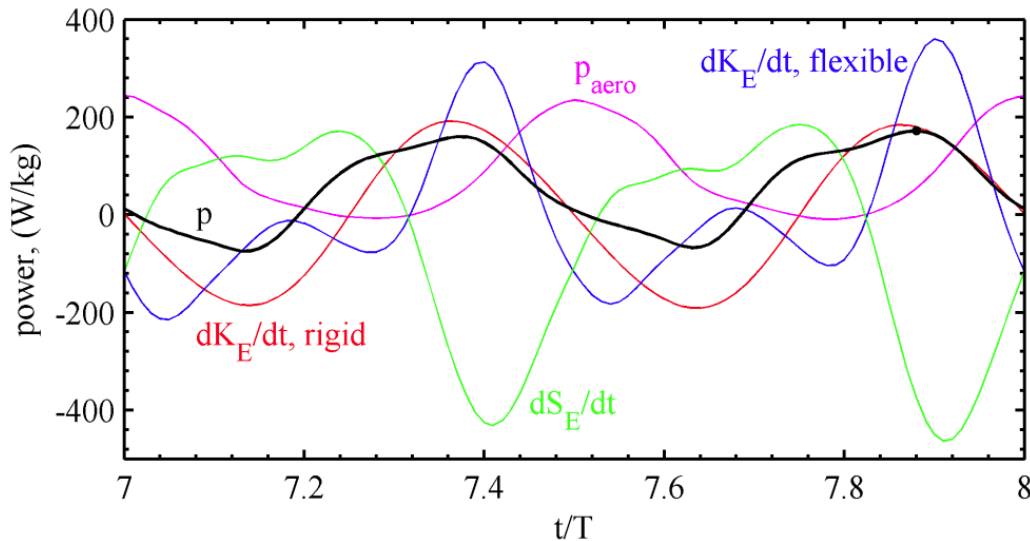


**Figure 13. Contributions to the power for optimal case C.**

The aeroelastic wing motion of case C is given in Figure 14, demonstrating the ability of the design to leverage aeroelastic deformation in a power-optimal manner. The commanded kinematics, as indicated by the rigid motion, provide a very small amplitude in both stroke motion  $\phi$  and stroke plane deviation angle  $\theta$ , thereby decreasing the inertial power requirement associated with the rigid motion,  $dK_E/dt$ . The resulting flexible motion substantially increases the amplitude of both angles, providing a wide figure-8 motion. As noted earlier, the feathering

motions  $\eta$  decreases the minimum angle of attack of the rigid wing. Such a rotation increases the stroke deviation, heightening the figure-8 for lift generation. This force development increases the aerodynamic power, but judicious phasing of the elastic energy storage within the cycle attenuates the peak.

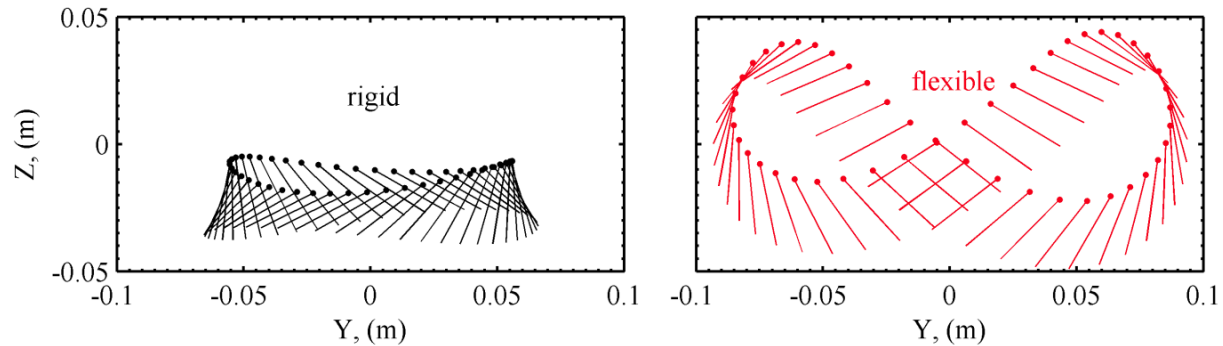


**Figure 14. Rigid and flexible motion of the wingtip for case C.**

In this application of an optimization strategy to understand the physics of flapping wings, three disparate types of design variables are considered: aerodynamic shape, wing structure, and kinematics. The optimization shows that judicious tailoring of the parameters creates beneficial interactions in the complex coupling of aerodynamics and structure, making it possible to reduce power requirements without compromising either lift generation for trim or structural integrity. The following conclusions can be drawn:

1. Flexible wing motion can differ substantially from the commanded kinematics enforced at the wing root, providing wider stroke angles, higher stroke velocities, and larger stroke plane deviations. Optimal designs rely upon large passive wing deformation to satisfy lift requirements.
2. Aerodynamic power requirements are typically positive, while inertial and elastic contributions are liable to be negative. The peak power can be reduced by properly timing the phase angle between the aerodynamic power and the strain and kinetic energy rates of the vibrating beam.
3. Changes to the shape and structure are far more effective at reducing power requirements than changes to the flapping kinematics.

These conclusions indicate the importance of treating a flapping wing MAV as an aeroelastic system. An aerodynamics-only or a structures-only treatment will miss important physical interactions that generate superior performance.

## **B. Conceptual Design of Compliant Mechanisms for Flapping Wings**

Flapping-wing MAVs are generally of such small scale and light weight that the mechanism used to actuate flapping cannot be isolated from the aeroelastic system. Aerodynamic and inertial loads on the wings are carried into the actuation mechanism through the wing attachment, where they can have a first-order effect on the behavior of the mechanism. For this reason, we believe

that mechanism design should be incorporated into the aeroelastic design process for physical exploration. In a preliminary step towards such an integrated capability, we considered the conceptual design of the actuator alone, while subjected to aerodynamic, inertial, and structural loads from attached flapping wings<sup>37</sup>.

### 1. Optimizing for Thrust Alone

The problem is illustrated in Figure 15. The compliant actuation mechanism is constrained to reside within a 2D box, shown in the figure by the grey square. The mechanism is attached to two wings at the upper left and right corners of the box and the wings are made to flap by applying a sinusoidal point load vertically at the bottom center of the box, as indicated by the applied force  $f_1$ . The forces  $f_2$  and  $f_3$  shown in the figure are fixed at zero. This produces a simple flapping motion within the plane of the actuator box that, if large enough, will produce a propulsive force perpendicular to the box that is sufficient to overcome vehicle drag.

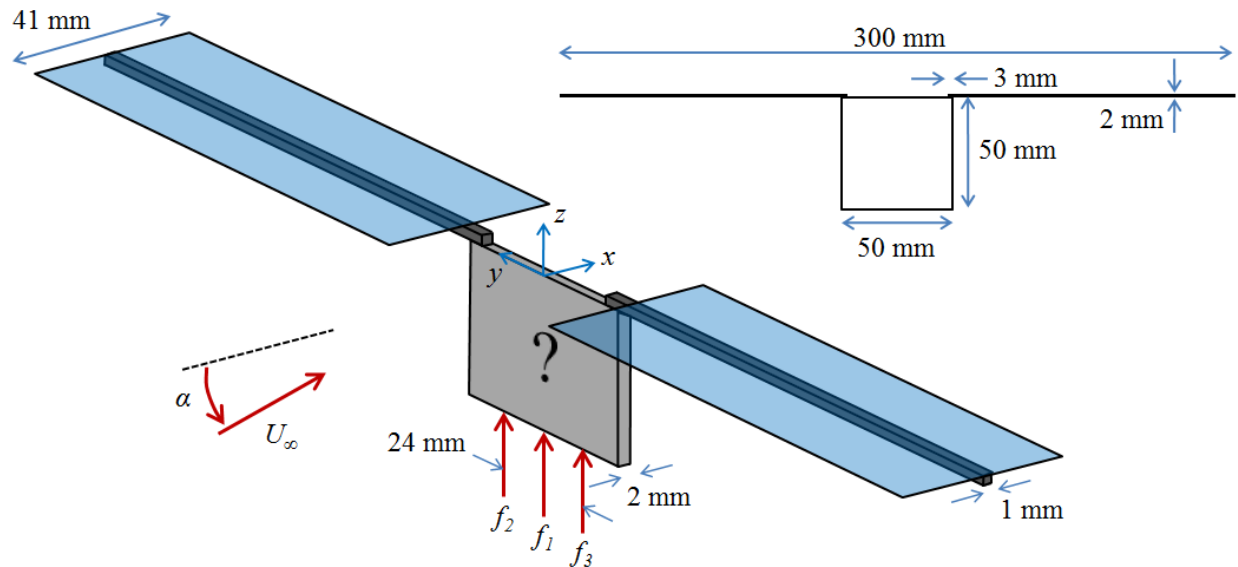


**Figure 15. Schematic of an actuated flapping wing in forward flight.**

The actuator design can be treated as a topological optimization problem in which the decision variables include both the mechanism topology and its supports. The optimization is expressed here in a gradient-based form and is solved using the method of moving asymptotes (MMA)<sup>38</sup>. The actuator region is divided into a number of elements and the MMA is allowed to choose the elements that will be occupied with material. The problem can be stated as follows:



$$\begin{aligned}
& \min_{\mathbf{x}, \mathbf{z}} (-C_{T,ave}) \\
& \text{s.t.} \\
& V(\mathbf{x}) \leq V^* \\
& S(\mathbf{z}) \leq S^* \\
& \mathbf{x}^T \cdot (1 - \mathbf{x}) \leq \text{grey}^* \\
& |u_n^{\text{in}}| \leq u^* \quad n = 1, \dots, N_{\text{steps}} \\
& x_{\min} \leq x_e \leq 1 \quad e = 1, \dots, N_e \\
& z_{\min} \leq z_e \leq 1 \quad e = 1, \dots, N_e
\end{aligned} \tag{13}$$

The objective is to maximize the cycle-averaged thrust coefficient  $C_{T,ave}$  while allowing the elemental densities  $\mathbf{x}$  and support variables  $\mathbf{z}$  to vary. The total volume  $V$  of the mechanism is required to be below some specified value and the area of support  $S$  is similarly required to fall below some value. It is further required that the magnitude of the displacement  $u^{\text{in}}$  at the input point load be less than some specified tolerance at each time step to stabilize the optimization and to provide a suitable load path between the input and the wing motion. An additional constraint on the elemental densities essentially drives the elements to binary empty or filled states. Lastly, side constraints are imposed on the decision variables.

Symmetry about the  $x$ - $z$  plane is assumed, so only half of the model need be modeled. The mechanism and the wing rod are idealized as a single finite element model, discretized into square Q4 elements that include geometrically nonlinear behavior to support large elastic deformations of slender structures<sup>39</sup>. Aerodynamic forces are applied to the nodes running along the lower surface of the wing rod. The wing is assumed to be perfectly rigid in both a chordwise and torsional sense so as to obtain a two-dimensional response; only external aerodynamic forces in the  $y$ - $z$  plane are applied to the structure. The material properties used for the structural model are shown in Table 4. The method of Buhl is used to support the design of the underlying support structure along with the topological design of the mechanism itself<sup>40</sup>. Within each bilinear element that falls within the actuator box, two springs are attached to each node and fixed points in space: one spring aligned horizontally and the other vertically. The stiffnesses of the eight springs are taken to be identical, and this value is used as a second design variable for the element, in addition to the element density. The blade element model of Berman and Wang is used to model the aerodynamic forces. Parameters describing the forward flight and blade element aerodynamic model are shown in Table 5. These parameters correspond to a Reynolds number of  $Re = 27,750$  and a reduced frequency based on the half-chord of  $k = 0.205$ . The final equations of motion resulting from the coupling of the structural and aerodynamic models form a second-order nonlinear differential equation. This is solved using an implicit time marching scheme with Newton-Raphson subiterations within each time step to drive the nonlinear residual below a specified tolerance.

The optimization algorithm requires sensitivities of the objective and constraint equations with respect to changes in the decision variables. A direct method is used here to evaluate these gradients analytically. This requires that a differential equation with multiple right-hand sides (one per decision variable) be integrated in time along with the system response. The Jacobian that is needed by this equation will be known from the system response computation at each time step. The Jacobian is fairly sparse and well banded, so the solution is not cumbersome.

Optimal topologies are shown in Figure 16. For cases 1 to 3, the underlying supports, shown in the figure with blue cross-hatching, were assumed and fixed. In cases 4 and 5, the support structure was designed simultaneously with the topology of the actuator. Within each of these problem types, the different optimal solutions represent different allowable volume fractions. All constraints were active for each design. Table 6 lists the key constraints and metrics for the optimal designs. The constraints are the volume fraction constraint  $V^*$  and the displacement constraint  $u^*$ , with maximization of the average thrust coefficient  $C_{T,ave}$  as the objective. From this table, it can be seen that cases 1 and 4 share the same volume and displacement constraints and differ only in the treatment of the supports. Cases 3 and 5 are similarly paired.

**Table 4. Structural parameters for the compliant actuation mechanism design.**

	Mechanism	Wing rod
Material	ABS plastic	Carbon fiber
Elastic modulus	2 GPa	40 GPa
Poisson's ratio	0.3	0.3
Density	1000 kg/m <sup>3</sup>	1400 kg/m <sup>3</sup>
Thickness	2 mm	1 mm
Failure stress	35 MPa (yield)	80 MPa (matrix cracking)
Damping, $\alpha_0$	5	5

**Table 5. Aerodynamic parameters for the compliant actuation mechanism design.**

Parameter	Value	Parameter	Value
Chord, $c$	4.1 cm	Angle of attack, $\alpha$	0°
Wing length, $l$	12.5 cm	Actuation force, $f$	15 N
Flow velocity, $U_\infty$	10 m/s	Frequency, $\omega$	100 rad/s
$\rho_f$	1.225 kg/m <sup>3</sup>	$\mu_1$	0.2
$C_{xz}$	$\pi$	$\mu_2$	0.2
$C_D(0)$	0.04	$\lambda_{x'}$	0 kg/m
$C_D(\pi/2)$	2	$\lambda_{y'}$	$1.671 \cdot 10^{-3}$ kg/m
$C_R$	$\pi$	$I_a$	$9.062 \cdot 10^{-8}$ kg-m

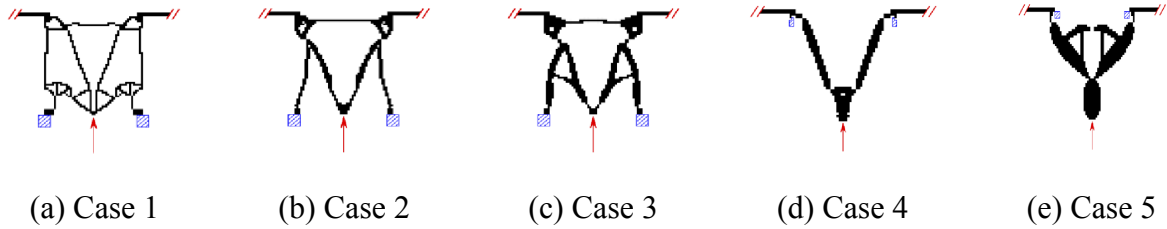


**Figure 16. Optimal topologies for a flapping-wing compliant actuation mechanism. Hatched areas are clamped. Cases 1-3 have fixed supports; cases 4 and 5 have variable supports.**

In case 1, an upwards applied force at the input port creates a positive moment about the wing joint, leading to a negative flapping angle and a downward motion of the wing tip. This behavior is also observed in the corresponding variable support design case 4. Cases 2, 3, and 5, which have larger volume fractions, exhibit opposite behavior: an upward force produces a positive flapping angle.

The variable support designs are simpler than the fixed support designs, with fewer moving parts and superior performance to the corresponding fixed support design. The variable support design of case 4 is, for example, exhibits roughly four times more thrust than the corresponding fixed support design of case 1. It is not clear what purpose the truss-like structure of case 5 serves, as it does not bear any stresses and does not appear to contribute to the kinematics. Potentially, this structure is an artifact of the optimization process and appears to fill out the volume constraint without adversely impacting the compliance of the mechanism.

**Table 6. Summary of performance metrics for optimal topologies for a flapping-wing compliant actuation mechanism**

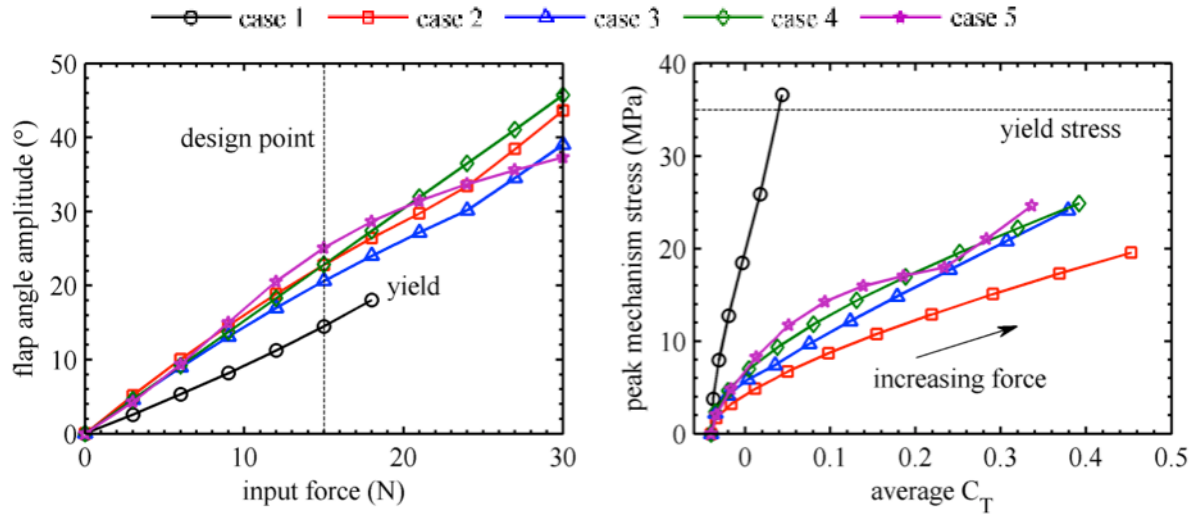
Constraints			Performance				
Case	$V^*$	$u^*$ (mm)	$C_{L,ave}$	$C_{T,ave}$	$C_{P,ave}$	$\sigma_{mech}$ (MPa)	$\sigma_{wing}$ (MPa)
1	0.170	2	0.0019	0.0178	0.0687	25.85	18.79
2	0.235	2	0.0042	0.0977	0.1129	8.68	27.62
3	0.300	2	0.0030	0.0735	0.0989	10.45	24.80
4	0.170	2	0.0015	0.0716	0.0980	11.65	26.58
5	0.300	2	0.0028	0.0909	0.1098	14.27	32.78

Changes in the behavior of the system for off-design actuation are shown in Figure 17 and Figure 18. For a fixed actuation frequency of 100 rad/sec, The left-hand plot in Figure 17 shows the effect of changes in the input force on the flapping amplitude. The design point of 15 N is shown in the figure by a dashed line. A monolithic relationship exists between the force and flapping rotation, with geometric nonlinearities and/or aerodynamic damping hardening the

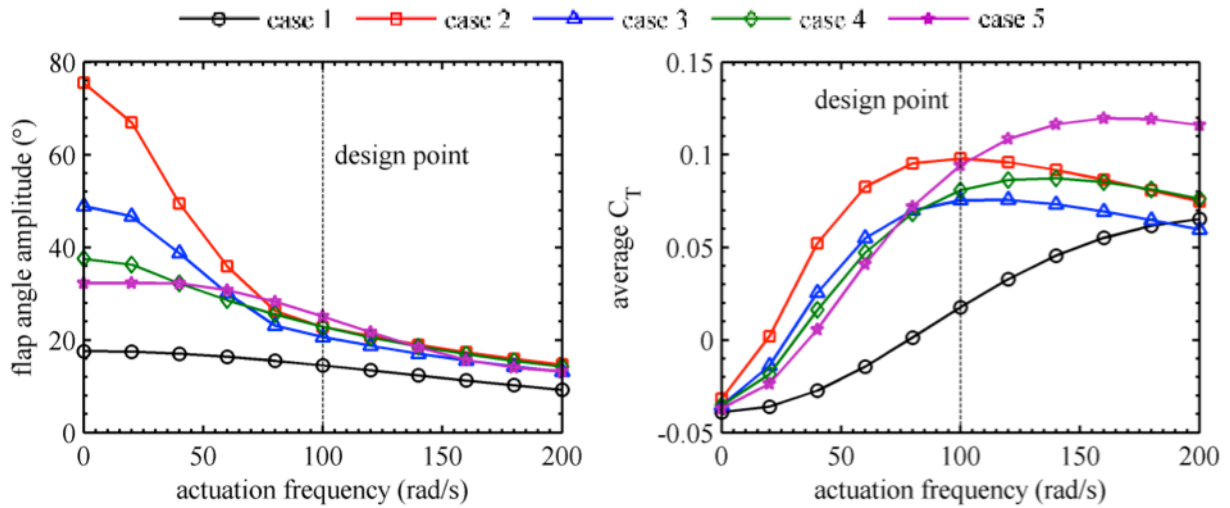
response under higher input forces. The right-hand plot in the figure shows the peak von Mises stress within the mechanism as a function of the cycle-averaged thrust coefficient. Each trend of this plot starts with zero input actuation, and so the only force present along the fixed flat-plate wing at zero angle of attack is the viscous drag. As such, each case starts with a thrust coefficient of  $-0.04$ , which is the specified  $C_D(0)$  from Table 5. The flapping motion initiates a thrust force that counteracts the drag. Each case is able to produce a net positive thrust except case 1. From the vantage point of Figure 17, case 2 is superior to the remaining designs in that it provides the highest level of propulsion with the lowest mechanism stresses, which should translate to a long fatigue life.

Figure 18 shows results of fixing the input actuation at 15 N and traces the response as a function of the actuation frequency. As this frequency approaches zero, the motion is quasi-steady and only the input and elastic forces contribute. The resulting deformation is large and nonlinear. In particular, case 2 flaps at an amplitude of  $75^\circ$ . For nonzero frequencies, the aerodynamic forces resist the motion and the inertial wing loads require a greater power input. The net result is a decreased effectiveness of the compliant mechanism with the introduction of aerodynamic and inertial loads, which has also been noted experimentally. The thrust data on the right of the figure begins at  $C_D(0)$  for the same reasons as above, and sees an initial quadratic growth with frequency. This growth is diminished, and eventually reversed, by the loss of flapping amplitude. It should be noted that this is strictly a coupled aeroelastic phenomena, which has also been observed experimentally; increasing the actuation frequency in a vacuum would result in a quadratic growth in thrust, eventually curbed by excessive geometric nonlinearities or inertial loads. From the vantage point of Figure 18, case 5 is superior and is able to achieve a high peak thrust in the high-frequency domain, although case 2 is the best at lower frequencies. The stresses for case 6 (not shown) are relatively low. Both effects are thought to be due to the rigid body-like motions emulated by this variable support topology, which is less susceptible to aerodynamic resistance and elastic failure.

The inclusion of geometrically nonlinear elastic forces, unsteady inertial forces, quasi-steady aerodynamic forces, and oscillating actuation forces into a gradient-based topology optimization scheme has produced compliant actuation mechanism designs that provide required levels of thrust while including the coupling that exists between the flapping wing and the mechanism itself. Modifying the constraint boundaries and the support details provides greater control over the stresses than topological optimization alone. This is an important consideration from a fatigue standpoint, where cyclic high-speed stresses can greatly reduce the expected life and reliability of a flapping aircraft. Variable supports, in particular, were shown to be effective for creating simple designs with few moving parts.



**Figure 17. Variation in flapping performance due to changes in compliant actuator input force ( $\omega = 100$  rad/sec).**



**Figure 18. Variation in flapping performance due to changes in compliant actuator input frequency ( $f = 15$  N).**

## 2. Optimizing for Thrust and Rolling Moment

The work described above assumes symmetric flapping motion and aims to maximize thrust production for efficient, sustained, steady, forward flight. This work has been extended to consider the optimization of a compliant mechanism designed to perform two tasks<sup>42</sup>. First, as before, the mechanism must be able to transform an input actuation force into symmetric flapping motions of left and right wings. The flapping amplitude must be large enough to produce sufficient thrust to overcome the aerodynamic drag and achieve sustained forward flight.

Second, under different actuation, the mechanism must be able to produce unsymmetric motion between the left and right wings that gives rise to an aerodynamic rolling moment. This will allow turning maneuvers. The topology of the mechanism itself must remain symmetric to facilitate the first goal, as well as to allow for equal capacity in left and right turns. These two goals are viewed as multiple load cases and are handled as a multi-objective optimization problem.

The geometry of the problem is that of Figure 15, but now the entire configuration must be modeled so as to include unsymmetric actuation and response. Input actuation forces may be applied according to one of two scenarios. In the first scenario, separate actuators are utilized for the symmetric and unsymmetric flapping motion. A single oscillating point load  $f_1$  acting along the centerline is used to generate symmetric motion. A single oscillating point load  $f_3$ , offset from the centerline, is used to produce unsymmetric motion. In the second scenario, equal oscillating point loads at  $f_2$  and  $f_3$  are used to produce symmetric flapping and a point load at  $f_3$  is again used to produce unsymmetric flapping. The two scenarios are shown graphically in Figure 19.

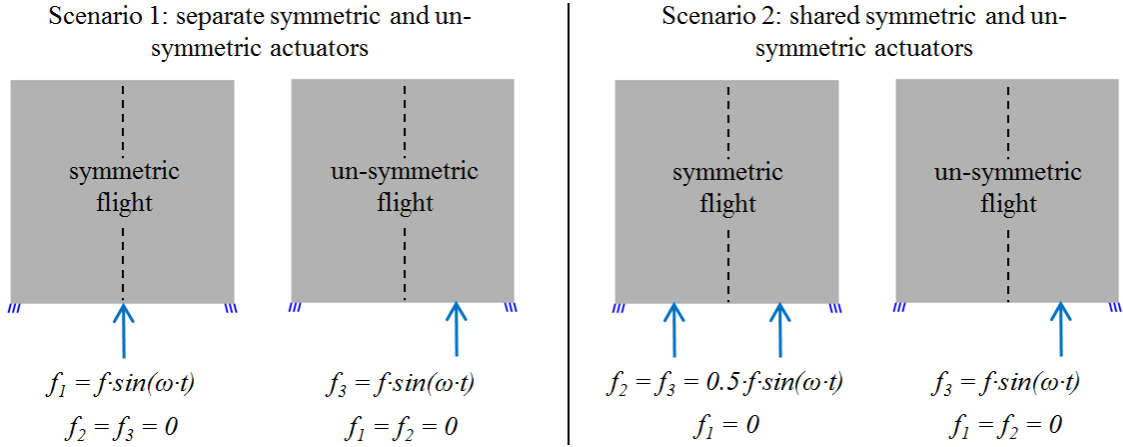


**Figure 19. Two scenarios for symmetric and unsymmetric actuation of left and right wings using a compliant mechanism.**

The optimization problem is slightly modified from the earlier statement:

$$\begin{aligned}
 & \min_{\mathbf{x}} (-C_{L,max}) \\
 & \text{s.t.} \\
 & C_{T,ave} \geq C_T^* \\
 & V(\mathbf{x}) \leq V^* \\
 & \mathbf{x}^T \cdot (1 - \mathbf{x}) \leq \text{grey}^* \\
 & |u_n^{\text{in}}| \leq u^* \quad n = 1, \dots, N_{\text{steps}} \\
 & x_{min} \leq x_e \leq 1 \quad e = 1, \dots, N_e
 \end{aligned} \tag{14}$$

Here it is desired to maximize the peak rolling moment coefficient  $C_L$  during the flapping cycle such that the cycle-averaged thrust coefficient is greater than or equal to some trim requirement. Taking  $C_T^* = 0$  indicates that the propulsive forces exactly cancel with the viscous drag. Also, we do not here consider the design of the support locations. The structural and aerodynamic parameters are those from Table 4 and Table 5, except that  $C_D(0) = 0.025$ .

Two cases are considered for each actuation scenario: one mechanism designed to a maximum volume fraction of  $V^* = 0.21$  and the other designed to a larger volume fraction of  $V^* = 0.28$ . The maximum rolling moment coefficients and cycle-averaged thrust coefficients obtained from the four optimal mechanisms are reported in Table 7. The mechanisms themselves are shown in Figure 20. In all designs, a positive input actuation force targeting symmetric motion produces an upward flapping motion in the wings, as with cases 2, 3, and 5 in the thrust-only optimization. For unsymmetric motion, a positive force on the right side of the mechanism produces an upward motion in the right wing. How the left wing reacts to this force governs the rolling moment performance of the mechanism, with larger unsymmetric behavior leading to larger rolling moments. In mechanism 1, the left wing does not respond significantly to actuation on the right side: the cross bracing between the two sides of the mechanism is too stiff to transmit the force across the mechanism. This can also be seen in Figure 21, which shows the relationship between the sinusoidal input loading and the flapping angle. For mechanism 1, there is a  $90^\circ$  phase lag between the input force and the wing motion. Mechanism 2 is observed to be stiff due to the higher volume fraction constraint, which drops the amplitude of the flapping motions and the associated aerodynamic flight metrics. The rolling moment, in particular, is less than that from mechanism 1, despite the fact that the wing motions are more unsymmetric. Also, it can be seen that the phase lag between the input and output is lower than that in mechanism 1, as the aerodynamic resistance is weaker. Mechanism 3, in which the symmetric and unsymmetric actuators are shared, provides the largest rolling moment coefficient of any design. However, the design is not successful at thrust production, with a lower cycle-averaged thrust coefficient than every other mechanism. This may be due to the fact that the topology has less connectivity between the input ports and the clamped boundary conditions than the other mechanisms and, thus, struggles to use these fixed points to convert the input forces into bending moments about the wing joints. This indicates a topological tradeoff between effectiveness in symmetric and unsymmetric flight. Mechanism 4, with a higher volume fraction constraint, has a better symmetric thrust coefficient than mechanism 3, but is too stiff in the unsymmetric sense, leading to a very small maximum rolling moment.

The mechanisms designed under scenario 2 are topologically simpler, but are less successful in generating aerodynamic thrust and rolling moments. From the multi-objective standpoint of being able to perform both tasks moderately well, mechanism 1 may be considered the superior design. From a manufacturing vantage, however, mechanism 3 may be preferred.

Several conclusions can be drawn from the results of the multi-objective compliant mechanism design study. First, mechanisms designed under high volume fraction constraints are too stiff and are unable to leverage deformations to produce substantial aerodynamic loads. Second, symmetric actuation is able to produce high thrust via large flapping amplitudes. Unsymmetric actuation, on the other hand, is more dependent on large discrepancies between the right and left wing motions to produce high rolling moments. Third, using the same actuators for

both symmetric and unsymmetric motion leads to topologically simpler designs, but are not as successful in robustly producing the desired aerodynamic loads as designs using separate actuators. Finally, successful operation under both symmetric and unsymmetric load cases suggests that it may be possible to smoothly control shifts between longitudinal and lateral flight.

**Table 7. Summary of optimal compliant actuation mechanisms designed for maximum rolling moment and a trimming cycle-averaged thrust coefficient.**

Mechanism	Scenario	$V^*$	Symmetric flapping		Unsymmetric flapping	
			$C_{L,max}$	$C_{T,ave}$	$C_{L,max}$	$C_{T,ave}$
1	1	0.21	$\sim 0$	0.0377	0.4891	0.0155
2	1	0.28	$\sim 0$	0.0047	0.3577	-0.0021
3	2	0.21	$\sim 0$	-0.0033	0.5224	0.0312
4	2	0.28	$\sim 0$	0.0028	0.0642	0.0034

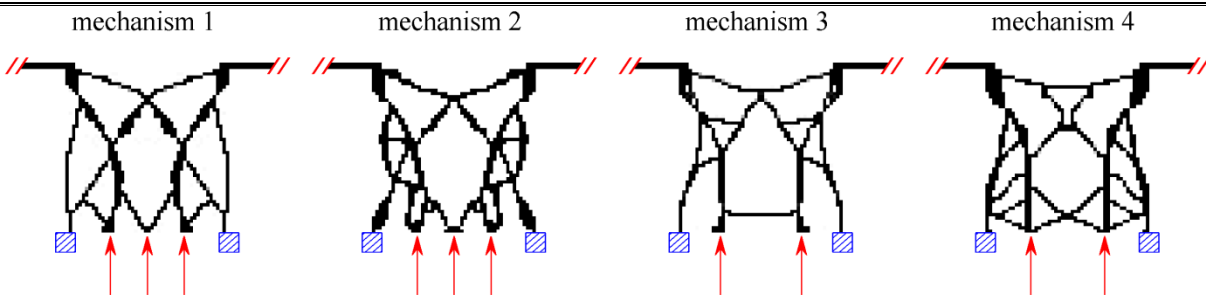


**Figure 20. Optimal compliant actuation mechanisms designed for maximum rolling moment and a trimming cycle-averaged thrust coefficient.**

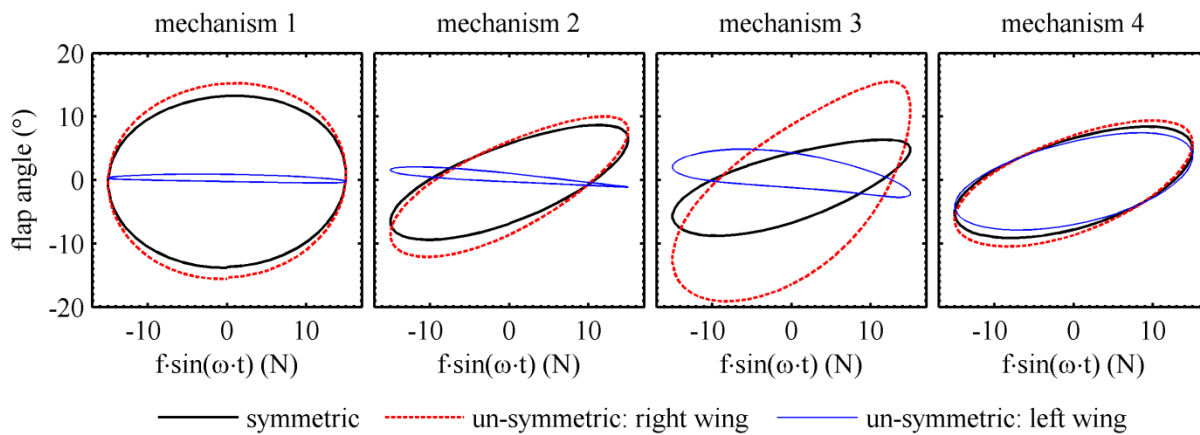


**Figure 21. Phase diagrams of flapping rotation due to input actuation (positive angles correspond to wing tips up).**



### C. Influence of Wing Stiffener Arrangements on Flapping Wing Performance

Inspired by nature, engineers often design mechanical flappers with wings composed of a thin, flexible membrane affixed to an underlying lattice of stiffeners. This type of wing is desirable for meeting stringent payload and power budget requirements. Careful selection of the stiffener pattern can provide additional aeroelastic benefits. Previous work in this area includes a description of the aerodynamic benefit of one skeletal arrangement over another<sup>44</sup>, characterization of the benefits of perimeter reinforcement for hovering wings<sup>45</sup>, and studies into the effects of variable spar stiffness distribution in a given wing topology<sup>46-48</sup>. These research efforts used experimental testing, but a comprehensive experimental study detailing the relationship between stiffener arrangements and flapping flight performance is probably impractical given the quantity and diversity of topologies that should be considered. A numerical optimization scheme offers a means to locate preferred membrane wing stiffener arrangements for a series of aerodynamic metrics, as well as identify the tradeoff curves that connect the disparate design objectives.

The conceptual design of the stiffener arrangement in a membrane wing is essentially a topological optimization problem. However, a solid isotropic material with penalization (SIMP) method such as that used above for compliant mechanism design is considered undesirable for this application because of the potential existence of multiple local minima and the need for difficult and costly gradient computations. Instead, the NSGA-II genetic algorithm is used because it offers gradient-free global multi-objective optimization. Three objectives are considered: maximizing cycle-averaged lift, maximizing cycle-averaged thrust, and minimizing the cycle-averaged power requirement.

The genetic algorithm acts on a genome that encodes a developmental program. When that program is compiled and executed, it uses a Lindenmayer system (L-system, for short) to develop a wing topology consisting of a set of connected closed membrane cells<sup>49</sup>. The edges of the cells are taken to be the structural stiffeners. By encoding a developmental program into the genome instead of a fine grid of potential stiffeners, the number of design variables may be kept relatively small while the attainable topologies can be extremely diverse. Also, each design variable has a global influence on the resulting topology and aeroelastic response, which makes crossover and mutation operations in the genetic algorithm more efficient.

An L-system is a parallel rewriting system, often used to model growth processes in plants<sup>50</sup>. Here, Binary Propagating Map 0L-systems with markers (mBPM0L-systems, for short) are used to define the membrane wing stiffener arrangement and to interface with the genetic algorithm for topology optimization. These are a subclass of L-systems. In a map L-system, the starting seed must form a closed cell. The method is further termed “binary” because the cells are required to divide in two during the division process, and “propagating” because cells cannot fuse together or disappear. The system is defined by a tuple  $\mathbf{G} = (V, \omega, P)$ , composed of an alphabet  $V$  that consists of a set of symbols, an axiom  $\omega$  that defines the initial state of the system, and a set of production rules  $P$  that define how variables change over time. Each production rule consists of predecessor and a successor strings, and these rules are applied simultaneously, once per iteration.

An example set of production rules is:

$$\begin{aligned}
A &\rightarrow B[+A]x[-A]B \\
B &\rightarrow A \\
x &\rightarrow x
\end{aligned} \tag{15}$$

Where the alphabet  $V = \{A \ B \ x\}$ . A production rule is assigned to each symbol in the alphabet, with an identity rule for  $x$ . Each letter outside the brackets specifies an edge subdivision, and the letter inside the brackets specifies a marker label for a possible cell division. The marker is placed to the left of the predecessor if a positive sign precedes the letter, and to the right if a negative sign precedes it. After markers have been placed, each cell is scanned for matching markers. When matching markers are found on different edges in a cell, they are joined to subdivide the cell and form a new edge. If more than one pair is found, the first pair found that creates angles and an area larger than some prescribed lower bound is used. Remaining markers are discarded. Starting from an axiom  $\omega = ABAB$ , Figure 22 shows the first four iterations of the method.

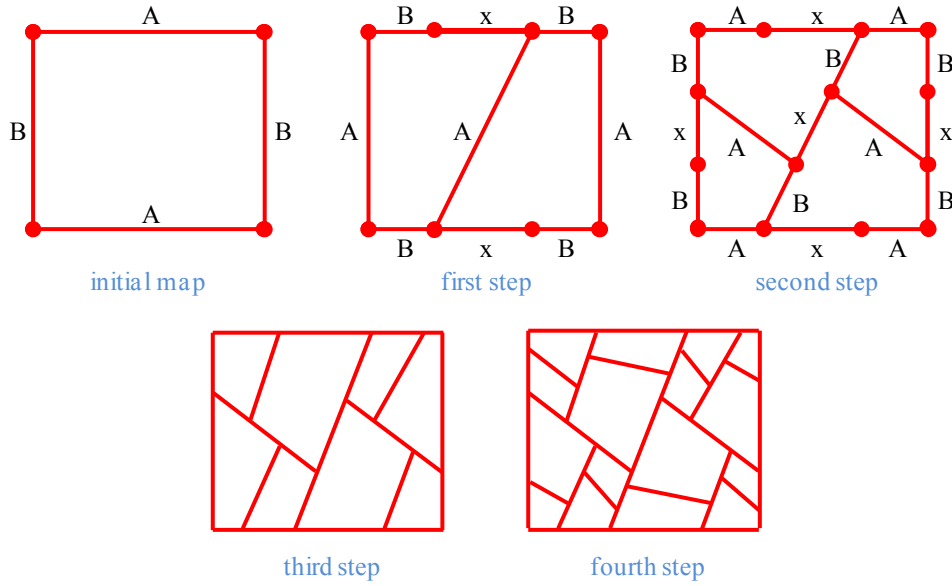


**Figure 22. First four iterations of an example cellular division process.**

The process can be terminated after each cell is smaller than some required area, after a defined maximum number of steps, or when the system becomes invariant with successive iterations.

The above cellular division method is used in conjunction with the genetic algorithm by encoding it into a vector of real numbers, which is used as the genome. The genome is partitioned as:

$$Y = \{Y_1^\omega \quad \dots \quad Y_m^\omega \quad Y_1^{P_1} \quad \dots \quad Y_n^{P_1} \quad \dots \quad Y_1^{P_k} \quad \dots \quad Y_n^{P_k}\} \tag{16}$$

where  $\{Y_1^\omega \ Y_2^\omega \ \dots \ Y_m^\omega\}$  encodes the axiom,  $\{Y_1^{P_1} \ Y_2^{P_1} \ \dots \ Y_n^{P_1}\}$  encodes the first production rule, and so on. Kobayashi and others provide methods by which symbols and production rules can be converted into real numbers<sup>51</sup>.

Once the final cellular division topology has been obtained, the square geometry is transformed into the space defined by the wing planform. The four outer cell walls become the leading edge, wing root, trailing edge, and wing tip. The edge vertices within the four outer walls are mapped into the wing planform, and the edges are redrawn to keep the stiffeners straight.

The wing is modeled structurally as a collection of triangular membrane elements with embedded Euler-Bernoulli beam elements. A typical wing is shown in Figure 23.

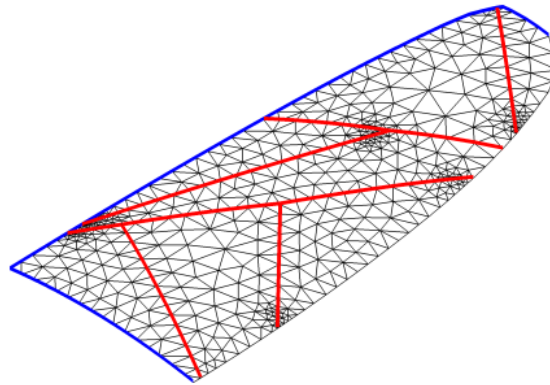


**Figure 23. Sample wing finite element model for studying the effect of stiffener arrangements on aeroelastic performance. Membrane elements are outlined with thin black lines and beam elements are shown as thick blue and red lines.**

This model can be considered accurate if the stresses that develop within the membrane as a result of the loading are smaller than the pre-stresses. This condition has been demonstrated by experimental validation for membrane wing skeletons<sup>52</sup>. Excessive deformation may require nonlinear membrane models, but this is not considered here. To reduce the cost of the system analysis, the solution vector is approximated as a linear combination of a relatively small number of natural vibration modes. The resulting structural equations of motion are of the form

$$\mathbf{M}_r \cdot \ddot{\boldsymbol{\eta}} + \mathbf{C}_r \cdot \dot{\boldsymbol{\eta}} + \mathbf{K}_r \cdot \boldsymbol{\eta} = \boldsymbol{\Phi}^T \mathbf{F} \quad (17)$$

The airloads are computed using Peters aerodynamics, which allows for coupling with a generic unsteady wake model and relies upon Glauert expansions to form matrix expressions analogous to Equation 17<sup>53</sup>. The method allows for large rigid body motions and small elastic deformations. The vehicle is inclined at fixed angle of attack relative to the incoming flow and the wings flap according to

$$h(t, x) = \sum_{n=0}^{\infty} h_n \cdot \cos(n\varphi) \quad (18)$$

where  $\varphi = \cos^{-1}(x/b)$  and  $x$  is in a local, body-attached reference frame. Peter's inflow theory is used to calculate the flow induced by the trailing wake<sup>54</sup>.

The coupled aerodynamic and structural equations are solved using a spectral element method that exploits the cyclic nature of the problem. The set of differential equations describing the aeroelastic system are converted into an algebraic set of monolithic time-periodic equations. This method is efficient and bypasses the initial transients of the system<sup>55,56</sup>. It is also possible to use *hp*-refinement for temporal accuracy and asymptotic annihilation<sup>57</sup>. The main drawback is that the final algebraic system of equations may be very large, equal to the product of the number of spatial and temporal degrees of freedom. Use of modal reduction for the structure helps alleviate this cost.

A Zimmerman planform with a root chord of 16 cm, a tip chord of 4 cm, and a wing length (root to tip) of 40 cm is used for the following results. This planform is shown in Figure 23. A constant parabolic arc airfoil section is used, with a peak camber of 2% of the local chord, no twist, and no dihedral. The wing is oriented at an angle of attack of  $\alpha = 4^\circ$ , the flow velocity is  $U_\infty = 10$  m/s, and the amplitude of the sinusoidal flapping motion is  $\beta = 30^\circ$  at a frequency of  $\omega = 40$  rad/s. The resulting reduced frequency is  $k = 0.32$  and the Reynolds number is  $Re = 10,000$ . The drag coefficients are set to  $C_{D0} = 0.05$  and  $C_{D\pi/2} = 2.0$ .

The wing is constructed from a thin latex membrane sheet adhered to a carbon fiber skeleton. The material properties are summarized in Table 8. The membrane is assumed to have an isotropic spatially uniform pre-tension and the skeleton is composed of a lattice of unidirectional laminate strips with rectangular cross sections. In order to investigate the effect of skeletal stiffness upon the optimal topological configuration, two cases are studied. The beam elements that make up the first quarter-chord of the root and the first quarter-chord of the leading edge are clamped in the body-attached coordinate system.

Three objective functions are considered: maximizing the cycle-averaged lift, maximizing the cycle-averaged thrust, and minimizing the cycle-averaged power consumption. The power is a sum of aerodynamic power, strain energy rate, and kinetic energy rate, though the first is most important for forward flapping flight, and the only one of the three that has a non-zero average over a cycle. No constraints are considered in the optimization. The procedure used to find the Pareto front spanning these three objectives is as follows. First, single-objective optimization runs are conducted with each objective. The three optimum designs are then combined with a population of several random designs to locate the three Pareto fronts spanned by the three dual-objective optimization problems. Finally, these fronts are combined with additional random designs to locate the three-objective Pareto front. A population size of 100 is used for the first two steps, and 300 is used for the final step, each with a maximum of 100 generations.

**Table 8. Material and geometric properties of the membrane wing and stiffeners.**

	Membrane	Flexible case		Stiff case	
		LE	Battens	LE	Battens
Elastic modulus, $E$ (MPa)	2	$3 \times 10^5$	$3 \times 10^5$	$3 \times 10^5$	$3 \times 10^5$
Poisson's ratio, $\nu$	0.5	0.34	0.34	0.34	0.34
Density, $\rho$ (kg/m <sup>3</sup> )	1200	1600	1600	1600	1600
Thickness (mm)	0.1	1.4	0.4	2.0	0.8
Width (mm)	—	5.0	1.0	5.0	3.0
Pre-stress, $N_x, N_y$ (N/m)	10	—	—	—	—

The resulting extremes of the final Pareto front for the flexible skeleton parameters are given in Figure 24, corresponding to the highest average thrust, the lowest average power, and the highest average lift. The relevant aerodynamic metrics are provided for each, as well as the cellular representation and the resulting wing topology. The propulsive efficiency  $\eta$  is also given, but is not used during the optimization. The topology of the peak thrust design is oriented for the wing to behave in a beam-like fashion. In contrast, the minimum power design is very sparse and flexible in a chordwise bending. The peak lift design is a combination of the two, with a distinct topological change at midspan.

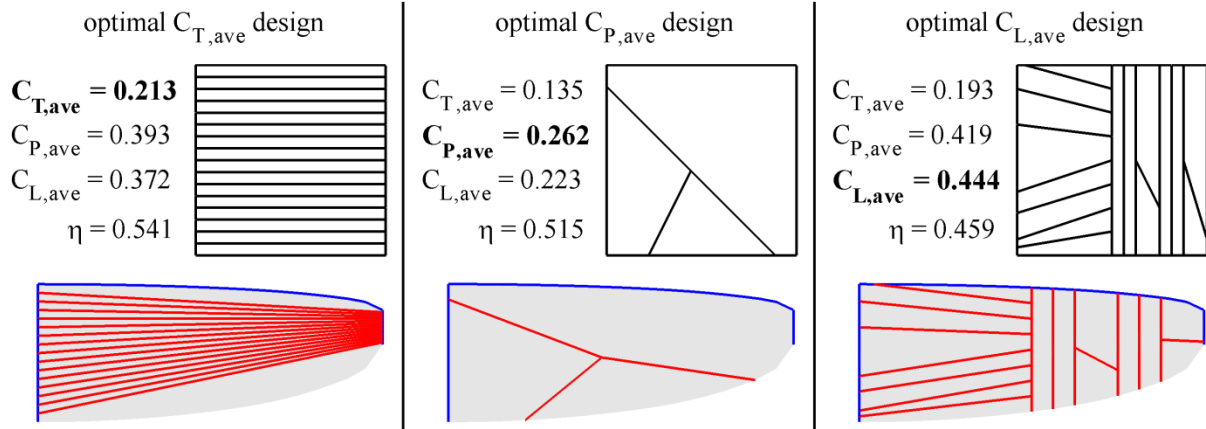


**Figure 24. Single-objective optimal designs for a flexible wing skeleton.**

The optimal topologies for the stiffer skeletal parameters are given in Figure 25. The thrust and power optimal designs are very similar to the flexible case. The lift-optimal design is, however, very different, with a large region of free membrane skin surrounded by battens. These differences indicate that cross-sectional properties should be included in the optimization along with the topology variables, so as to fully exploit the aeroelastic behavior.

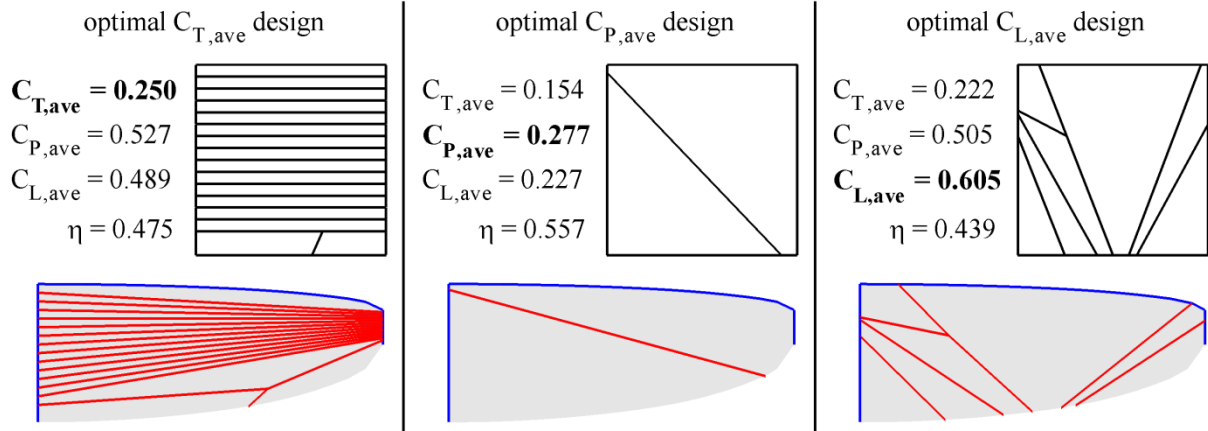


**Figure 25. Single-objective optimal designs for a stiff wing skeleton.**

Figure 26 and Figure 27 show the thrust-power Pareto fronts for both the flexible and stiff cases, respectively. Several topologies are given along the fronts, showing the gradual transition from diagonally oriented minimum power design to spanwise maximum thrust design. Uniformly distributed random designs are also plotted. In the flexible case, all of the random designs are densely clustered just behind the Pareto front, indicating that off-optimal designs perform comparably to optimal designs. Contrastingly, in the stiff case, many of the designs are well removed from the front, in general, and the single-objective optimal designs, in particular. This indicates that careful selection of the wing stiffener arrangement can have a significant impact on performance when the support skeleton contributes substantially to the total mass and stiffness of the wing and, therefore, has a significant influence on aeroelastic behavior of the wing.

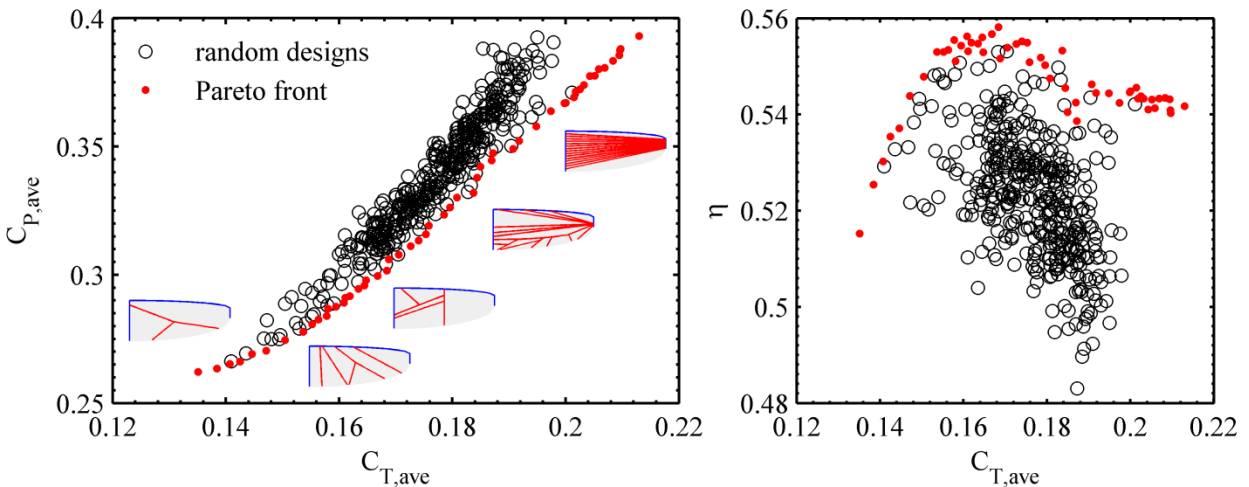


**Figure 26. Thrust-power Pareto front for the flexible case.**

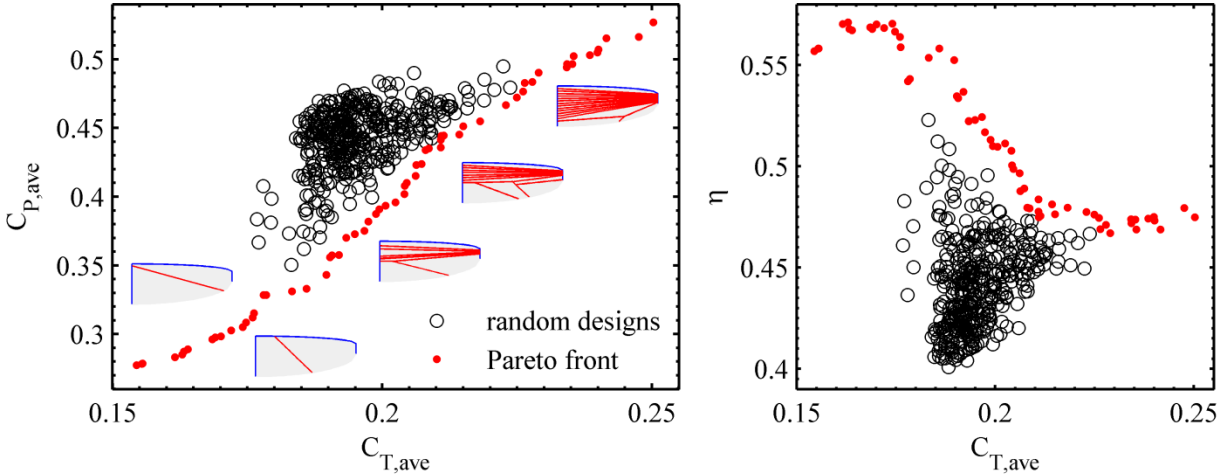


**Figure 27. Thrust-power Pareto front for the stiff case.**

Since the wing topologies with stiffer battens have a more diverse design space and greater need for optimization, only this configuration will be considered further. The three-objective Pareto front is shown in Figure 28. Projections of the front into the lift-thrust and thrust-power planes are also given. It can be observed in this figure that the tradeoff between lift and thrust is not as clearly defined as that between power and thrust. Designs with high lift tend to also have high thrust, and so the conflict between these two objectives is not strong. Power requirements for flapping can, however, typically be lowered by reducing the aerodynamic resistance as much as possible, which clearly conflicts with the generation of lift and thrust.

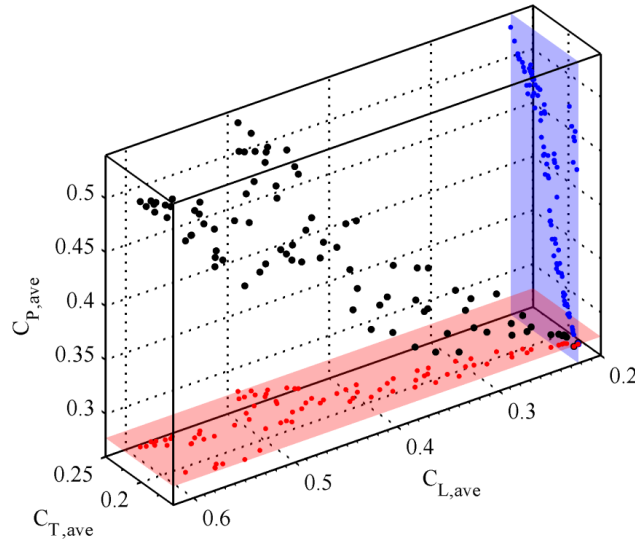


**Figure 28. Thrust-power-lift Pareto front for the stiff configuration.**

The aeroelastic response of the thrust-optimal case is shown in Figure 29, which includes nine snapshots of the wing throughout the flapping stroke. One side shows a translucent rigid

wing and a contoured flexible wing, where the contour is the out-of-plane displacement. The other side shows the flexible wing stiffener arrangement. The deformation patterns for this case are dominated by a spanwise bending mode whose deformations are moderately in-phase with the flapping motion. As the wing travels downward through the midstroke, the rigid body velocity is augmented with a downward deformational velocity, increasing the local lift vector. The angle of attack tilts this vector forward, resulting in increased thrust. The phase lag between the deformation and rigid flapping is large enough, however, to ensure that a portion of the wing is in motion at all times, preventing the development of drag. Stanford and Beran note a similar phenomenon with regards to thrust-optimal plunging shells<sup>58</sup>.

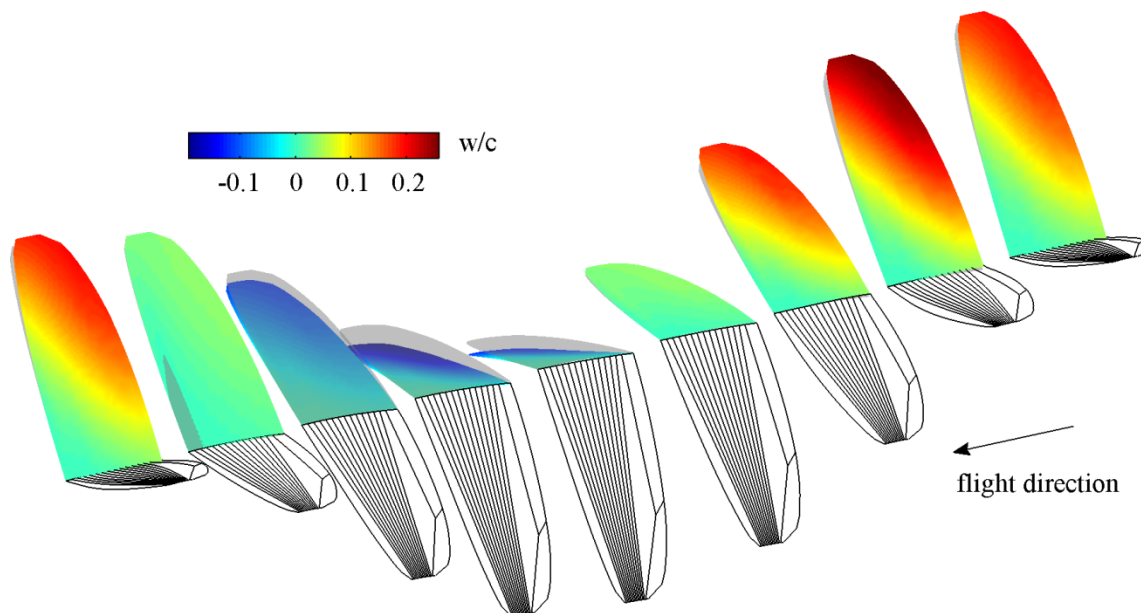


**Figure 29. Out-of-plane wing deformation throughout the flapping cycle of the thrust-optimal stiff topology design.**

The power-optimal design requires less than half of the peak power than that of the lift- and thrust-optimal designs, but suffers from potentially unacceptable drops in lift and thrust, with the former particularly severe. The aeroelastic deformations that cause these shifts in aerodynamic loading are shown in Figure 30. A large adaptive washout of the trailing edge occurs as the wing travels downward through the midstroke, which is a direct result of the minimal support provided by the single diagonal batten running through the wing. The chordwise wing deformation attempts to align each wing section with the flow so as to reduce the aerodynamic resistance and, consequently, the power draw. Adaptive wash-in occurs as the wing travels upward through the midstroke, though the trailing edge deformation is less.



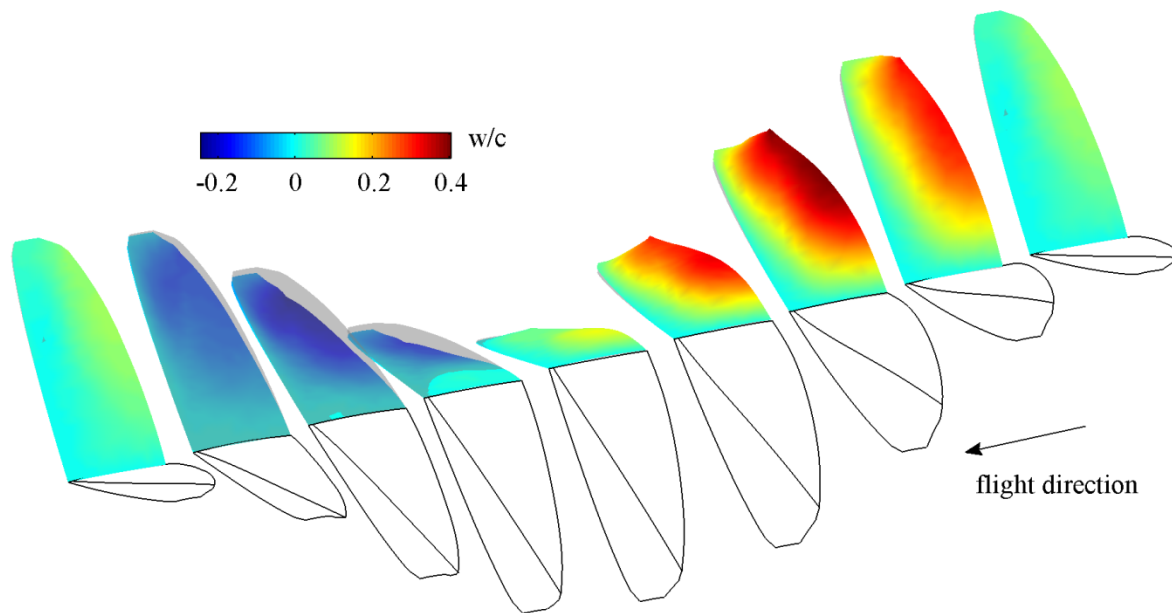


**Figure 30. Out-of-plane wing deformation throughout the flapping cycle of the power-optimal stiff topology design.**

Though unsteady effects can lead to phase shifting, peak inertial loads are expected at stroke reversal, where rigid body wing acceleration is largest. Peak aerodynamic loads occur through the midstroke, where the wing velocity is largest. The power-optimal wing exploits the latter, as the small deformation at stroke reversal and the sparse skeletal topology both indicate small inertial loads. The thrust-optimal design, however, appears to have an equal presence of both inertial and aerodynamic loads, due to the relative magnitudes of deformation at the midstroke and at stroke reversal, as well as the dense batten topology. The relative importance of aerodynamic and inertial loads in biological flight has long been debated<sup>59</sup>. The current results would indicate that the system might exploit either to achieve the desired aerodynamic metrics.

The aeroelastic design for the lift-optimal configuration corresponds to large force production, with the highest lift, thrust, and power history peaks. The deformations over a flapping cycle are shown in Figure 31. A large triangular portion of the wing is composed of a free membrane surface, constrained along most of its border by stiff battens. This membrane inflates during the downstroke, increasing the camber and the resulting lift force. Similar aeroelastic topology optimization strategies have been noted concerning the use of perimeter-reinforced membranes for lift production<sup>60</sup>. As with the thrust-optimal design, inertial loads don't have a significant role in the optimal fluid-structure interaction of this design.

This application combines a cellular division algorithm and a genetic optimization algorithm with an efficient aeroelastic model to study the effect of stiffener arrangements on the performance of a flapping-wing vehicle in forward flight. Examination of the topologies obtained along the Pareto front and their associated aeroelastic behavior provided insights into aeroelastic mechanisms that can be exploited through careful selection of stiffener layout to improve performance. Spanwise bending, adaptive washout, and adaptive cambering can be used

to select a desirable tradeoff between thrust and lift production and power consumption. The relative importance of inertial and aerodynamic loads was also seen to be dependent on the design objectives.

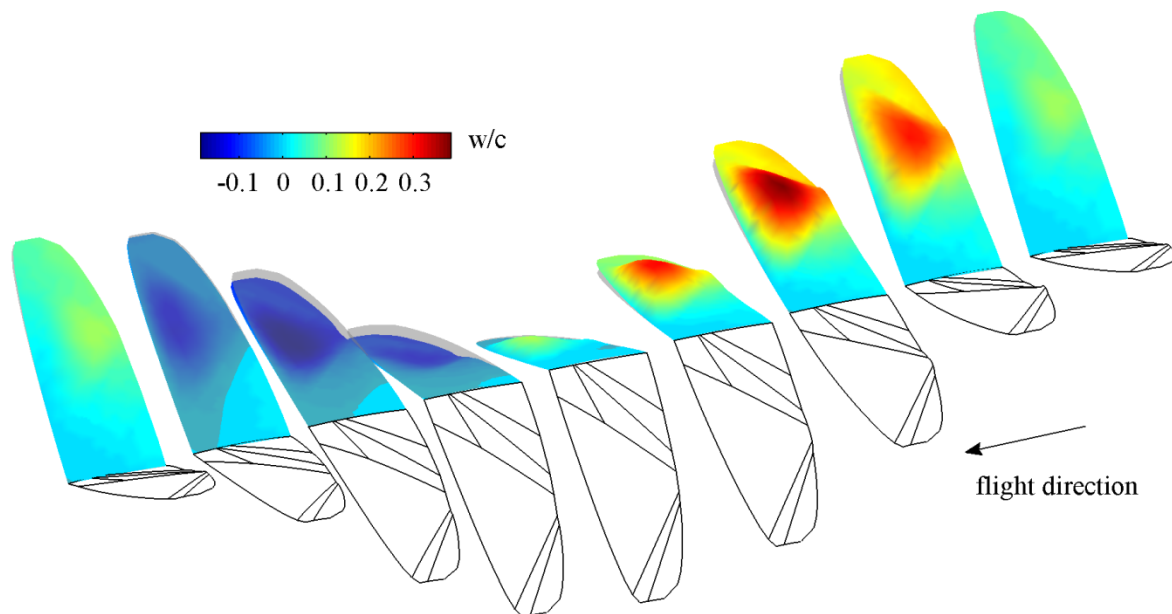


**Figure 31. Out-of-plane deformation throughout the flapping cycle of the lift-optimal stiff topology design.**

## CONCLUSIONS

The “Physics-based Design of Micro Air Vehicles” laboratory task has produced several unique studies into the key system parameters and underlying physical interactions that drive efficient performance of flapping-wing MAVs. These studies consistently support the conclusion that aeroelastic and multidisciplinary effects are indispensable to the performance of this class of aircraft. Furthermore, we have demonstrated the utility of optimization methods as a means for exploring large parameter spaces to discover performance-enhancing physical interactions. Once the optimization process identifies interesting parameter combinations, more costly, high fidelity methods can be used to verify the discovered phenomenon and provide details missed by the lower-fidelity design methods.

The optimization strategy must be tailored to meet the unique needs of each application. The physical modeling should provide sufficient fidelity to capture the essential physical phenomena, yet fast enough to permit evaluation at many points in the parameter space of interest. For this reason, we rely on a stable stocked with methods from a variety of disciplines, suitable for a range of configurations and fidelity. Methods can be drawn from this stable and harnessed, as appropriate, for each application. Throughout, methods that are tailored to exploit features of the response, such as time periodicity, or that provide analytic sensitivities are favored for their speed and accuracy.

We have applied the optimization strategy to problems involving small-scale, flapping aircraft operating in either hover or forward flight. These have focused on key interactions between the unsteady aerodynamics and underlying structure and topology. The first application sought out beneficial combinations of shape, structure, and kinematics for a flapping wing in hover. This work demonstrates that peak power can be reduced by carefully controlling the relative contributions to total power from aerodynamics, inertia, and structural deformation. The second application produced insight into appropriate topologies for compliant mechanisms that might be used to actuate wing flapping. Results indicate that the flapping actuator cannot be isolated from the aeroelastic system describing the wing; they should be designed together. The third application studied the impact of stiffener arrangement in a membrane wing on various performance indicators. This study reveals that aeroelastic tailoring can be used to vary the relative importance of aerodynamic and inertial loads to achieve a desired tradeoff of lift and thrust production and power consumption.

Our goal for follow-on work is to build a detailed and quantitative understanding of the influence of system configuration and flight atmosphere on the controllability and agility of small, uninhabited, fixed- and flapping-wing aircraft. This will involve a combination of experimental and computational research. The experimental work will focus on the characterization of gust and turbulence and their effects on small aircraft operating in close and urban environments. The computational research will build on our strategy of using multidisciplinary optimization as a means of exploring large parameter spaces characterized by complex, nonlinear interactions. These computations will involve coupled aerodynamics, structure, controls, and kinematics.

## **ACKNOWLEDGMENTS**

The Air Force Office of Scientific Research sponsored this work under Laboratory Task 09RB01COR, monitored by Dr. Douglas Smith.

## REFERENCES

1. AeroVironment, Inc. "Aerovironment Develops World's First Fully Operational Life-Sized Hummingbird-Like Unmanned Aircraft for DARPA," Press release, 2011.
2. Berman, G. and Wang, Z., "Energy-Minimizing Kinematics In Hovering Insect Flight," *Journal of Fluid Mechanics*, Vol. 582, 2007, pp. 153—168.
3. Kurdi, Mohammad, Beran, Philip S., Stanford, Bret K., and Snyder, Richard D., "Optimal Actuation of Nonlinear Resonant Systems," *Structural and Multidisciplinary Optimization*, Vol. 41, No. 1, February 2010, pp. 65—86.
4. Kurdi, Mohammad, Stanford, Bret K., and Beran, Philip S., "Optimal Kinematics of Hovering Insect Flight for Minimum Mechanical Power," AIAA-2010-1420, *48th AIAA Aerospace Sciences Meeting and Exhibit*, Orlando FL, 4-7 January 2010.
5. Andersen, A., Pesavento, U., and Wang, Z. J., "Unsteady Aerodynamics of Fluttering and Tumbling Plates," *Journal of Fluid Mechanics*, Vol. 541, 2005, pp. 65—90.
6. Pesavento, U. and Wang, Z. J., "Falling Paper: Navier-Stokes Solutions, Model of Fluid Forces, and Center of Mass Elevation," *Physical Review Letters*, Vol. 93, No. 14, 2004, pp. 1445011—1445014.
7. Snyder, Richard D., Chabalko Christopher C., and Beran, Philip S., "Two-Dimensional Flapping Wing Stroke Kinematics," IFASD-2009-164, *2009 International Forum on Aeroelasticity and Structural Dynamics*, Seattle WA, 22-24 June 2009.
8. Stanford, Bret K., and Beran, Philip S., "Analytical Sensitivity Analysis of an Unsteady Vortex Lattice Method for Flapping Wing Optimization," *Journal of Aircraft*, Vol. 47, No. 2, March-April 2010, pp. 647—662.
9. Sytsma, Michael J. and Ukeiley, Larry, "Low Order Turbulence Modeling Methods for MAVs Flight Environment," AIAA-2010-7935, *AIAA Aircraft Flight Mechanics Conference*, Toronto, Canada, 2-5 August 2010.
10. Karamcheti, K., *Principles of Ideal-Flow Aerodynamics*, Krieger Publishing Company, Cambridge MA, 2nd ed., 1980.
11. Katz, J. and Plotkin, A., *Low-Speed Aerodynamics*, Cambridge University Press, Cambridge MA, 2006.
12. Chabalko, Christopher C., Snyder, Richard D., Beran, Philip S., and Parker, Gregory H., "The Physics of an Optimized Flapping Wing Micro Air Vehicle," AIAA-2009-0801, *47th AIAA Aerospace Sciences Meeting and Exhibit*, Orlando FL, 5-8 January 2009.
13. McClung, Aaron M., Stanford, Bret K., and Beran, Philip S., "High-Fidelity Models for the Fluid-Structure Interaction of a Flexible Hovering Flapping Wing," AIAA-2010-

2959, *51st AIAA/ASME/ASCE/AHS/ASC Structures, Structural Dynamics, and Materials Conference*, Orlando FL, 12-15 April 2010.

14. Nichols, R. H. and Buning, P. G., "OVERFLOW 2 Training Class: Flow Solver Overview," *8th Symposium on Overset Composite Grids and Solution Technology*, Houston TX, 2006.
15. Nichols, R. H., Tramel, R. W., and Buning, P. G., "Evaluation of Two High Order WENO Schemes," AIAA-2007-3920, *25th AIAA Applied Aerodynamics Conference*, Miami FL, 25-28 June 2007.
16. Pandya, S. A., Venkataswaran, S., and Pulliam, T. H., "Implementation of Preconditioned Dual-Time Procedures in OVERFLOW," AIAA-2003-72, *41st AIAA Aerospace Sciences Meeting and Exhibit*, Reno NV, 6-9 January 2003.
17. Buning, P. G. and Nichols, R. H., "OVERFLOW 2 Training Class: Moving Body Capability," *8th Symposium on Overset Composite Grids and Solution Technology*, Houston TX, 2006.
18. Heathcote, S. and Gursul, I., "Flexible Flapping Airfoil Propulsion at Low Reynolds Numbers," *AIAA Journal*, Vol. 45, No. 5, 2007, pp. 1066—1079.
19. Balaras, E. and Yang, J., "Nonboundary Conforming Methods for Large-Eddy Simulations of Biological Flows," *Journal of Fluids Engineering*, Vol. 127, No. 5, 2005, pp. 851—857.
20. Dong, H., Harff, M., and Mittal, R., "Vortex Structures and Aerodynamic Performance of Finite-Aspect-Ratio Flapping Wings in Hovering Motion," AIAA-2007-4210, *37th AIAA Fluid Dynamics Conference and Exhibit*, Miami FL, 25-28 June 2007.
21. Ramakrishnan, S., Zheng, L., Mittal, R., Najjar, F., Lauder, G. V., and Hedrick, T. L., "Large Eddy Simulation of Flows with Complex Moving Boundaries: Application to Flying and Swimming in Animals," AIAA-2009-3976, *19th AIAA Computational Fluid Dynamics Conference*, San Antonio TX, 22-25 June 2009.
22. Yu, W., *VABS Manual for Users*, 3.4 ed., 2011.
23. Yu, W., Volovoi, V. V., Hodges, D. H., and Hong, X., "Validation of the Variational Asymptotic Beam Sectional Analysis," *AIAA Journal*, Vol. 40, No. 10, 2002, pp. 2105—2112.
24. Stanford, Bret K., and Beran, Philip S., "Cost Reduction Techniques for the Structural Design of Nonlinear Flapping Wings," *International Journal for Numerical Methods in Engineering*, March 2011.
25. Stanford, Bret K., and Beran, Philip S., "Optimal Structural Topology of a Flat Plate-Like Wing for Subsonic Aeroelastic Stability," AIAA-2010-2841, *51st AIAA/ASME/ASCE/*

*AHS/ASC Structures, Structural Dynamics, and Materials Conference*, Orlando FL, 12-15 April 2010.

26. Stanford, Bret K., and Beran, Philip S., “An Updated Lagrangian Shell and Vortex Lattice Aeroelastic Framework for Flapping Wings,” IFASD-2009-140, *International Forum on Aeroelasticity and Structural Dynamics*, Seattle WA, 22-24 June 2009.
27. Khosravi, P., Ganesan, R., and Sedaghati, R., “Corotational Non-Linear Analysis of Thin Plates and Shells Using a New Shell Element,” *International Journal for Numerical Methods in Engineering*, Vol. 68, 2007, pp. 859—885.
28. Chimakurthi, S. K., Cesnik, C. E. S., and Stanford, B. K., “Flapping-Wing Structural Dynamics Formulation Based on a Corotational Shell Finite Element,” *AIAA Journal*, 2011, Vol. 49, No. 1, 2011, pp. 128—142.
29. Stanford, Bret K., Kurdi, Mohammad, Beran, Philip S., and McClung, Aaron M., “Shape, Structure, and Kinematic Parameterization of a Power-Optimal Hovering Wing,” AIAA-2010-2963, *51st AIAA/ASME/ASCE/AHS/ASC Structures, Structural Dynamics, and Materials Conference*, Orlando FL, 12-15 April 2010.
30. Berman, G. and Wang, Z., “Energy-Minimizing Kinematics in Hovering Insect Flight,” *Journal of Fluid Mechanics*, Vol. 582, 2007, pp. 153—168.
31. de Boor, C., *A Practical Guide to Splines*, Applied Mathematical Sciences 27, Springer, revised ed. 1978.
32. Vanderplaats, G. N., *Numerical Optimization Techniques for Engineering Design*, 3rd ed., Vanderplaats Research & Development, Inc., 1999.
33. Vanderplaats, G. N., *DOT Design Optimization Tools: Users Manual*, Version 5.0, Vanderplaats Research & Development, Inc., 2001.
34. Deb, K., Agrawal, S., Pratap, A., and Meyarivan, T., “A Fast Elitist Non-Dominated Sorting Genetic Algorithm for Multi-Objective Optimization: NSGA-II,” *Parallel Problem Solving from Nature PPSN VI, Lecture Notes in Computer Science*, Vol. 1917, 2000, pp. 849—858.
35. Combes, S., and Daniel, T., “Flexural Stiffness in Insect Wings I. Scaling and the Influence of Wing Venation,” *Journal of Experimental Biology*, Vol. 206, 2003, pp. 2979-2987.
36. Bryson, Dean E. and others, “Multidisciplinary Optimization of a Hovering Wing with a Service-Oriented Framework and Experimental Model Validation,” AIAA-2011-1133, *49th AIAA Aerospace Sciences Meeting*, Orlando FL, 4-7 January 2011.
37. Stanford, Bret K., “Conceptual Design of Compliant Mechanisms for Flapping Wings with Topology Optimization,” *AIAA Journal*, Vol. 49, No. 4, April 2011 pp. 855-867.

38. Svanberg, K., "The Method of Moving Asymptotes: A New Method for Structural Optimization," *International Journal for Numerical Methods in Engineering*, Vol. 24, No. 2, 1987, pp. 359—373.
39. Zienkiewicz, O., *The Finite Element Method*, McGraw-Hill, New York, 1972.
40. Buhl, T., "Simultaneous Topology Optimization of Structure and Supports," *Structural and Multidisciplinary Optimization*, Vol. 35, No. 5, 2006, pp. 525—545.
41. Wu, P., Stanford, B., and Ifju, P., "Flapping Wing Structural Deformation and Thrust Correlation Study with Flexible Membrane Wings," *AIAA Journal*, Vol. 48, No. 9, 2010, pp. 2111-2122.
42. Stanford, Bret K., and Beran, Philip S., "Optimal Compliant Flapping Mechanism Topologies with Multiple Load Cases," AIAA-2011-2091, *52nd AIAA/ASME/ASCE/AHS/ASC Structures, Structural Dynamics and Materials Conference*, Denver CO, 4-7 April 2011.
43. Stanford, Bret K., Beran, Philip S., and Kobayashi, Marcelo, "Aeroelastic Optimization of Flapping Wing Venation: A Cellular Division Approach," AIAA-2011-2094, *52nd AIAA/ASME/ASCE/AHS/ASC Structures, Structural Dynamics and Materials Conference*, Denver CO, 4-7 April 2011.
44. Ho, S., Nassef, H., Pornsinsirak, N., Tai, Y., and Ho, C., "Unsteady Aerodynamics and Flow Control for Flapping Wing Flyers," *Progress in Aerospace Sciences*, Vol. 39, No. 8, 2003, pp. 635-681.
45. Singh, B. and Chopra, I., "Insect-Based Hover-Capable Flapping Wings for Micro Air Vehicles: Experiments and Analysis," *AIAA Journal*, Vol. 46, No. 9, 2008, pp. 2115-2135.
46. Hu, H., Kumar, A., Abate, G., Albertani, R., "An Experimental Investigation on the Aerodynamic Performances of Flexible Membrane Wings in Flapping Flight," *Aerospace Sciences and Technology*, Vol. 14, 2010, pp. 575-586.
47. Mazaheri, K. and Ebrahemi, A., "Experimental Study on Interaction of Aerodynamics with Flexible Wings of Flapping Vehicles in Hovering and Cruise Flight," *Archive of Applied Mechanics*, Vol. 80, 2010, pp. 1255-1269.
48. Wu, P., Stanford, B., Sallstrom, E., Ukeiley, L., Ifju, P., "Structural Dynamics and Aerodynamics Measurements of Biologically Inspired Flexible Flapping Wings," *Bioinspiration and Biomimetics*, Vol. 6, No. 1, 2011, 016009.
49. Kobayashi, M., Pedro, H., Kolonay, R., and Reich, G., "On a Cellular Division Method for Aircraft Structural Design," *The Aeronautical Journal*, Vol. 113, No. 1150, 2009, pp. 821-831.



50. Rozenberg, G. and Salomaa, A., *The Mathematical Theory of L Systems*, Academic Press, New York, 1980.
51. Kobayashi, M., "On a Biologically Inspired Topology Optimization Method," *Communications in Nonlinear Science and Numerical Simulation*, Vol. 15, No. 3, 2010, pp. 787-802.
52. Stanford, B., Albertani, R., and Ifju, P., "Static Finite Element Validation of a Flexible Micro Air Vehicle," *Experimental Mechanics*, Vol. 47, No. 2, 2007, pp. 283-294.
53. Peters, D., Hsieh, M., and Torrero, A., "A State-Space Airloads Theory for Flexible Airfoils," *Journal of the American Helicopter Society*, Vol. 51, No. 4, 2007, pp. 329-342.
54. Peters, D., Karunamoorthy, S., and Cao, W., "Finite State Induced Flow Models, Part I: Two-Dimensional Thin Airfoil," *Journal of Aircraft*, Vol. 32, No. 2, 1995, pp. 313-322.
55. Kurdi, M. and Beran, P., "Spectral Element Method in Time for Rapidly Actuated Systems," *Journal of Computational Physics*, Vol. 227, No. 3, 2008, pp. 1809-1835.
56. Kurdi, Mohammad, Beran, Philip S., and Snyder, Richard D., "Work-Amplitude Optimal Actuation of Nonlinear Resonant System," AIAA-2008-6075, *12th AIAA/ISSMO Multidisciplinary Analysis and Optimization Conference*, Victoria BC, 10-12 September 2008.
57. Stanford, B., Beran, P., and Kurdi, M., "Adjoint Sensitivities of Time-Periodic Nonlinear Structural Dynamics via Model Reduction," *Computers and Structures*, Vol. 88, No. 19, 2010, pp. 1110-1123.
58. Stanford, Bret K., "Formulation of Analytical Design Derivatives for Nonlinear Unsteady Aeroelasticity," *AIAA Journal*, Vol. 49, No. 3, March 2011 pp. 598-610.
59. Combes, S. and Daniel, T., "Into Thin Air: Contributions of Aerodynamic and Inertial-Elastic Forces to Wing Bending in the Hawkmoth *Manduca sexta*," *Journal of Experimental Biology*, Vol. 206, 2003, pp. 2999-3006.
60. Stanford, B. and Ifju, P., "Aeroelastic Topology Optimization of Membrane Structures for Micro Air Vehicles," *Structural and Multidisciplinary Optimization*, Vol. 38, No. 3, 2009, pp. 301-316.